Applied Catalysis A, General 651 (2023) 119033

Contents lists available at ScienceDirect

Applied Catalysis A, General

journal homepage: www.elsevier.com/locate/apcata

On the stability of Ni/γ-Al_2O_3 catalyst and the effect of H_2O and O_2 during biogas reforming

Prakash V. Ponugoti [a], Priya Pathmanathan [b], Jyotsna Rapolu [a], A. Gomathi [b], Vinod M. Janardhanan [a,*]

[a] Department of Chemical Engineering, Indian Institute of Technology Hyderabad, Telangana 502 284, India
[b] Department of Chemistry, Mahindra University, Telangana 500043, India

ARTICLE INFO

Keywords:
Biogas
Reforming
CO_2
Catalyst
Deactivation

ABSTRACT

This work systematically studies the effect of process conditions on catalyst stability during biogas reforming to syngas. To study the effect of different oxidizer content and temperature on reforming reactions, appropriate ratios of H_2O/CH_4, O_2/CH_4, and operating temperatures are identified using chemical equilibrium analysis. Reactions are performed on 10 wt% Ni/γ-Al_2O_3 in a fixed bed reactor at different WHSVs. Reactions performed at high WHSV and 600–800 ˚C reveal catalyst deactivation at high steam content. The observed deactivation of the catalyst is due to the loss of active nickel sites because of sintering, carbon deposition, and the formation of inactive spinel. The addition of O_2 even in a small quantity improves the catalyst stability. The catalysts are characterized using XRD, FTIR, TPR, BET, TGA, XPS, and TEM.

1. Introduction

Biogas produced by microbial decomposition of organic matter under anaerobic conditions contains varying amounts of CH_4 (50–75%) and CO_2 (25–45%) as major constituents. Depending on the feedstock, it may also have minor quantities of H_2O, O_2, N_2, H_2, NH_3, and H_2S [1]. This carbon-neutral CH_4 source can be converted to syngas using steam, dry, and oxidative reforming processes. However, carbon deposition is one of the challenges associated with some of these reforming methods. High steam to carbon (S/C) ratio enhances the kinetics of carbon gasification, and therefore, carbon deposition during steam reforming of methane (SRM) can be suppressed by operating at a high S/C ratio (2 ~ 4); however, this comes at the cost of large pre-heater and reforming units. Syngas production through dry reforming of methane (DRM) is particularly attractive as it fixes two greenhouse gases, CO_2 and CH_4. However, this reaction is more endothermic and prone to carbon deposition than SRM. The higher endothermicity is due to the stable C-O bond (≈ 530 kJ/mol) in CO_2 and the coking results from CH_4 cracking beyond 557 ˚C and the Boudouard reaction below 700 ˚C. Due to the endothermic nature, SRM and DRM require operating temperatures in the range of 700–1000˚C for high CH_4 conversions. On the other hand, catalytic partial oxidation (CPoX) of methane is exothermic; its large-scale industrial adaptation is limited by the requirement of an air separation unit for pure O_2 production and the downstream O_2 separation to inhibit the fire hazard of oxygen-enriched mixtures [2]. Syngas, produced by these reforming processes, is the starting point for downstream processing of commodity chemicals and hydrocarbon fuels. The H_2/CO ratio typically required for forming C_{2+} oxygenates is 1.3 [3]. The formation of methanol is favored at higher ratios, however, selectivities to higher alcohols, hydrocarbons, and aldehydes increase with decreasing H_2/CO (ca. 0.5) [4]. Commercial Fischer-Tropsch (FT) chemistry using iron and cobalt catalysts requires a range of syngas composition of (0.6–1.7) and (2.0–2.15) respectively [5]. However, the individual operation of SRM, DRM, and CPoX are inconsequential in addressing these varying syngas compositions. Therefore, combined reforming processes such as auto thermal reforming (ATR) [6,7], combined steam and dry reforming of methane (CSDRM) [8], and tri-reforming of methane (TRM) [9,10] may serve the need.

Tri-reforming is a synergistic combination of methane reacting with three oxidants, viz. CO_2, H_2O, and O_2 simultaneously. The energy requirement for the endothermic SRM and DRM is met by the exothermic CPoX. Furthermore, resilience towards the catalyst deactivation from coke deposition through methane decomposition ($CH_4 \rightarrow C + 2\,H_2$, $\Delta H^0 = 74.9$ kJ/mol) and Boudouard ($2CO \rightleftharpoons C + CO_2$, $\Delta H^0 = -172.2$ kJ/mol) reactions can be increased by the steam gasification of coke ($C + H_2O \rightleftharpoons CO + H_2$, $\Delta H^0 = 131.4$ kJ/mol) and coke oxidation (C

* Corresponding author.
E-mail address: vj@che.iith.ac.in (V.M. Janardhanan).

https://doi.org/10.1016/j.apcata.2023.119033
Received 28 September 2022; Received in revised form 22 December 2022; Accepted 9 January 2023
Available online 11 January 2023

$+ O_2 \rightarrow CO_2$, $\Delta H^0 = -393.7$ kJ/mol) reactions [11–13]. Water gas shift is another reaction that accompanies the reforming reactions. However, the kinetics of this reaction is very fast and is considered to be in partial equilibrium.

Although methane reforming on different transition metals is reported in the literature, Ni is still the most preferred catalyst due to its low cost and reasonably good activity. Ni immobilized on supports such as Al_2O_3, CeO_2, ZrO_2, and MgO acts as an active phase for dehydrogenation reactions [14,15]. Still, its long-term stability is compromised by the deactivation mechanisms such as (i) carbon deposition, (ii) thermal sintering, (iii) inactive phase formation (solid-solid reactions), (iv) gas-solid reactions, and (v) catalyst poisoning [9]. In addition to the feed composition, temperature, pressure conditions, and the active catalyst, the support in acid and base catalysis also alters the product distribution during reforming reactions. Accordingly, the application of amphoteric oxide Al_2O_3 for TRM in its unaided support form is very limited [16–19]. While the basic oxides CeO_2, ZrO_2, MgO, and LaO both in their unaided form and as a support modifier for alumina have been extensively investigated [20–23,17,24].

Yoo et al. studied the effect of mesoporous 20 wt% Ni/Al_2O_3 synthesized using supercritical CO_2 and evaporative drying through the sol-gel method for DRM, SRM, CPoX, and TRM [16]. Supercritical CO_2 drying resulted in an aerogel catalyst (NAA) with a better specific surface area, average pore size, high methane adsorption capacity, and well dispersed active catalyst compared to xerogel catalyst (NAX) obtained through evaporative drying. Accordingly, enhanced catalytic activity w.r.t H_2 yield and CH_4 conversion were observed for NAA catalyst than NAX. The effect of support and metal support interaction (MSI) achieved through varying calcination temperatures was investigated by Kumar et al. for the application in TRM using industrial flue gases [18,19]. Reported results indicate superior catalytic activity of Ni/Al_2O_3 in comparison to SBA-15, MgO, CeO_2, ZrO_2, and TiO_2 as supports. The higher activity results from smaller active particle size, high Ni dispersion, and strong MSI due to elevated calcination temperatures (ca. 900–950˚C) [18,19].

Though tuning MSI increases the catalytic activity in harsh oxidative environments such as in TRM usage of steam accelerates the thermal sintering processes of small crystalline particles [25–27]. Compared to the bulk metal surfaces, increased surface energy or chemical potential of small particles (nanometers range) is the main driving force for the sintering processes, which occurs through particle migration or atom migration (Ostwald ripening). Accordingly, Sehested et al., through experimental and modeling studies, have reported that the formation of Ni_2-OH dimers increases at the surface due to hydroxyl radicals in the presence of steam [28–30]. At lower temperatures (< 600˚C) and ambient pressures, the Ni_2-OH complexes enhanced the surface mass transport of the nickel particles resulting in particle migration and coalescence [28]. However, the sintering mechanism depends on the operating conditions. Instead of low temperature and ambient pressures, if the condition changes to 600˚C and 40 bar or 650–750˚C at ambient pressure with high oxidant-reductant ratio ($p_{H_2O}/p_{H_2} = 50$) the sintering mechanism changes from particle migration to atom migration. Furthermore, at high temperature (ca. 750 ˚C) and $p_{H_2O}/p_{H_2} = 50$, in addition to the Ostwald ripening the steam-induced metal support interaction results in the formation of $NiAl_2O_4$; further reducing the accessible catalytic sites [29]. Nickel re-oxidation in high oxidative environments is another major contributing factor to the catalytic activity loss [18,19,31]. SRM under stoichiometric conditions results in p_{H_2O}/p_{H_2} below 0.1 when methane conversion exceeds 91%. However, coke suppression by co-feeding steam in excess of stoichiometric requirement results in increased p_{H_2O}/p_{H_2} ratio. Wolf et al., through size-dependent stability of metal nanoparticle studies at stoichiometric SRM feed conditions, have shown that Ni inhibits the re-oxidation when the particle size is > 3 nm. Furthermore, they also reported the presence of $NiAl_2O_4$ at elevated p_{H_2O}/p_{H_2} ratios [31].

Structural and morphological changes associated with sintering and re-oxidation phenomena are omnipresent in TRM, but their effect on catalyst deactivation can be addressed through redispersion strategies. Hence metal site reactivation through repeated oxidation and reduction cycles using O_2 and H_2 has been reported to regain the catalyst activity [32–35]. Despite the understanding of nickel redispersion studies, its application in non-stoichiometric feed conditions is not widely reported, especially in higher oxidative environments of TRM, which is relevant to the biogas reforming studies. Reported TRM studies in the available literature either uses sub-stoichiometric [18,19,22] or near stoichiometric [16,24,36] oxidant to fuel ratios to study the fouling of the catalyst with a H_2O/CH_4 always ≤ 0.6. Luneau et al. conducted the reforming studies of model biogas ($CH_4/CO_2 = 1.5$) at 700˚C on different Ni-based catalysts at high oxidant to fuel ratio ≈ 4.15 (S/C = 3, O/C = 0.5) [37,38]. Their results indicate the presence of a catalyst hot spot due to CH_4 combustion at the inlet of the bed and its propagation throughout the bed leading to catalyst deactivation. The reason for the observed deactivation is due to the formation of NiO followed by the formation of the inactive spinel structure, however, the latter compound is only observed in the post-reaction sample analysis [38]. The absence of NiO can be attributed to the stoichiometry of the freshly prepared catalyst as pointed out by Ubaid et al [39]. Ubaid et al. prepared stoichiometric (33 wt%), deficient (16 wt%), and excess (49 wt%) Ni-containing spinels for SRM and reported different Ni species to contribute to the deactivation. During SRM, Ni deficient catalyst is deactivated due to the reincorporation of Ni into inactive Ni-aluminate without any traces of NiO being observed. While in the case of excess Ni, the formed metallic Ni re-oxidized as appeared in the XRD pattern causing the catalyst to deactivate [39].

Therefore, this work aims to understand the significant role of deactivation mechanisms such as Ni-reoxidation, carbon deposition, and thermal sintering during the reforming of biogas. Specifically, the effect of steam on the thermal sintering and Ni-reoxidation of active metal is investigated by performing the reactions at different temperatures and S/C ratios. At the same time, the effect of catalyst deactivation due to carbon deposition is studied by using high-grade synthetic biogas feed ($CH_4/CO_2 = 2$). By varying the O_2/CH_4 ratios in the reaction mixture the specific cases of Ni-reoxidation and surface carbon oxidation were studied. Thermal sintering and its mitigation due to O_2 induced metal-redispersion is also investigated. Accordingly, the relative significance of these deactivation mechanisms on different CH_4 reforming reactions such as DRM, SRM, CSDRM, and TRM are studied by performing kinetic investigations on $Ni/\gamma\text{-}Al_2O_3$ catalyst synthesized using solution combustion synthesis (sol-gel) method. Reaction parameters such as CH_4 conversion (X_{CH_4}), CO_2 conversion (X_{CO_2}), and H_2/CO were used to monitor the performance of the catalyst, while its deactivation is measured in terms of drop in the conversion of CH_4 on time on stream.

2. Experimental and theoretical methods

2.1. Materials

Reagent grade Aluminium nitrate ($Al(NO_3)_3 \cdot 9\,H_2O$, $> 98\%$) and Nickel nitrate ($Ni(NO_3)_2 \cdot 6H_2O$, $> 99\%$) are used as metal precursors. For the modified Pechini method, citric acid anhydrous ($C_6H_8O_7$, $> 99.5\%$) is used as fuel, ethylene glycol ($C_2H_6O_2$, $> 99\%$) as a esterification agent, and ammonia solution (NH_4OH, 28–30%) for maintaining the pH. Ethylene glycol and Aluminium nitrate were procured from Merck, while the rest are from Sigma-Aldrich.

2.2. Catalyst preparation

10 wt% $Ni/\gamma\text{-}Al_2O_3$ is synthesized by following the modified Pechini (sol-gel) method. Accordingly, citric acid is used as a chelating agent to modify the hydrolysis chemistry of metal ions. Citric acid (CA) is a weak triprotic acid (H_3A), and its deprotonation depends upon the solution pH, as shown in Fig. S1 [40]. The homogeneity of the formed phase

depends on the initial metal ion concentration ($[M^{x+}]$), $[CA]/[M^{x+}]$ molar ratio, and pH of the starting solution, especially when mixed metals (Ni^{2+}, Al^{3+}) are involved [41,42]. A theoretical investigation to identify the optimal values of $[M^{x+}]$ (0.2 M, 0.4 M), $[CA]/[M^{x+}]$ (0.5, 1.0, 1.5, 2.0), and pH (0.0–10.0) is carried out using Visual MINTEQ software. The optimal parameters are selected by identifying the combined (Ni, Al) pH regions free from non-chelated metal ions and corresponding saturation index values for any possible precipitation. The optimal parameters chosen for the catalyst preparation are $[M^{x+}] = 0.2$ M, $[CA]/[M^{x+}] = 2.0$, and pH = 4.0–4.7 as shown in Fig. S2 (Calculations for $[CA]/[M^{x+}] = 0.5$, 1.0, 1.5 and $[M^{x+}] = 0.4$ M are not presented).

The synthesis procedure starts with the preparation of 0.2 M aqueous solutions for each metal separately, followed by the addition of citric acid while maintaining the ratio of $[CA]/[M^{x+}] = 2$. These aqueous solutions are then subjected to slow titration using ammonium hydroxide to attain a pH range of 4.0–4.7. At this point, Ni and Al clear sol are mixed, and ethylene glycol is added as an esterification agent. This enables the entrapping of metal ions (M^{x+}) into the covalent polymer network formed by the transesterification reaction between metal citrates and ethylene glycol (EG), thus avoiding the segregation of metals during heat treatment. For a complete esterification reaction to occur, EG is added to the sol in the molar ratio of EG/CA = 1.5. Later the sol is heat treated at 80˚C for excess water to evaporate, followed by the aging of the remaining viscous gel for three days resulting in a polymeric resin. To enhance the kinetics of the esterification reaction, the resulting polymeric resin was heated at 180˚C followed by calcination in a muffle furnace at 800 ˚C for 6 hours.

2.3. Equilibrium calculations

Thermodynamic chemical equilibrium analysis provides a yardstick for the per-pass conversion and the reaction mixture composition at the thermodynamic equilibrium. Consequently, an informed decision can be made in identifying the operating conditions for the process needs. To identify the optimum reaction conditions of the catalytic TRM process at a fixed $CH_4/CO_2 \approx 2$ (high-grade biogas composition), inlet feed molar ratios as specified in Table 1, and temperature are identified as operating variables. The pressure is fixed at 1 atm, and the temperature is varied from 500 to 1000˚C. Surface carbon is considered as one of the products for the equilibrium calculations.

Figures S3, S4, S5 and S6 show the major trends from the analysis based on the gasphase moles and their summary is provided in Table 2. Equilibrium results are analyzed to identify the operating variables maximizing the CH_4 and CO_2 conversions (X_{CH_4}, X_{CO_2}) for a product molar ratio of $H_2/CO \approx 2$. In the temperature range of 700–800˚C for $CH_4/CO_2 \approx 2$, a S/C = 0.88 results in a $H_2/CO = 2.07$. Addition of oxygen (O/C = 0.1) decreases the H_2/CO ratio to 1.93 as shown in Fig. S5, which is suitable for FT-Chemistry. As changes in the S/C ratio have an inverse effect between X_{CO_2} and X_{CH_4}, H_2/CO (cf. Table 2) a minimum S/C = 0.88 is used throughout this study and accordingly the optimum conditions (S/C, O/C) are identified as (0.88, 0.00) and (0.88, 0.10) for CSDRM and TRM respectively.

Table 1
Discrete combinatorial search space of H_2O/CH_4 (S/C) and O_2/CH_4 (O/C) molar ratios at $CH_4/CO_2 = 2$.

O/C	S/C	S/C	S/C	S/C	S/C
0.0	0.0	0.88	1.17	1.47	1.77
0.1	0.0	0.88	1.17	1.47	1.77
0.3	0.0	0.88	1.17	1.47	1.77
0.5	0.0	0.88	1.17	1.47	1.77

Table 2
Equilibrium calculations summary.

	X_{CH_4}	X_{CO_2}	H_2/CO	C†
S/C* ⇑	↗	↓	↑	↓
O/C* ⇑	↗	↓	↗	↓
T * ⇑	↑	↑	↓	↓

† Moles of carbon formed per moles of CH_4 in the feed. * Effect of the decision variable while others kept constant. ⇑ Increasing decision variable. ↑ Strong positive, ↓ Strong negative, ↗ Weak positive relationship with decision variable.

2.4. Catalyst characterization

Specific surface area, pore volume, and pore size distribution of Ni/γ-Al_2O_3 were calculated using a physisorption analyzer (Micromerticis ASAP 2020). Initially, the catalyst was degassed by subjecting to vacuum conditions (10^{-5} Torr) at 250˚C for 4 h to remove any physisorbed impurities and residual moisture/gases. The adsorption and desorption isotherms were recorded using the multipoint N_2 physisorption studies at − 196˚C. The adsorption isotherm data in the relative pressure (p/p_0) range of 0.05–0.3 and the Braunauer-Emmett-Teller (BET) equation were used for the specific surface area (m^2/g) calculation. In contrast, the adsorbed liquid N_2 quantity at $p/p_0 = 1.0$ was considered for average pore volume (cm^3/g) calculation. Barret-Joyner-Halenda (BJH) and the *t*-plot method were used for estimating pore size distribution and micropore area and volume, respectively.

Powder X-ray diffractogram (XRD) studies on fresh and spent catalysts were performed using a diffractometer (Rigaku Smart Lab) equipped with a monochromatic CuKα radiation source ($\lambda = 1.5418$ Å) operating at 45 kV and 30 mA under ambient conditions. XRD patterns were recorded in the range of $2\theta = 10^{\circ}$ to 85˚ with a scan rate of 3˚/min. Identification of crystallographic phases of the fresh and spent catalyst was accomplished using the ICDD (International Centre for Diffraction Data) database. Mean crystallite size (d) was estimated from the Scherrer equation ($d = k\lambda/\beta\cos(\theta)$) by utilizing the X-ray broadening (β) of Ni (111) planes.

Temperature programmed reduction (H_2-TPR) provides information about the influence of support material, reducible species, and catalytic pre-treatment conditions. H_2-TPR was performed using a chemisorption analyzer (Micromeritic AutoChem II 2920). Prior to the analysis, the calcined sample was pretreated at 250˚C to remove any impurities or residual moisture/gases under the argon (Ar) flow (20 ml/min) for one hour. Maintaining the Ar flow, the sample was cooled down to 100˚C followed by heating (10˚C/min) the sample to 850˚C in a 10 vol% H_2/Ar flow. The H_2 consumption was measured using a conventional thermal conductivity detector (TCD).

The Fourier infrared spectra (FTIR) of the fresh and spent catalysts were recorded in the transmission mode using Bruker TENSOR 37 FTIR spectrometer. To study the functional groups, the analysis was conducted in the wavelength range of 400–4000 cm^{-1} with a scan resolution of 4 cm^{-1} and an average of 256 scans under ambient conditions. Prior to analysis, the sample was mixed with spectroscopic grade KBr and pelletized into a transparent circular wafer. All the recorded spectra were taken against a KBr background performed under similar conditions.

Analysis of carbonaceous deposits on fresh and spent catalysts was studied using a thermogravimetric analyzer (TA Instruments SDT Q600). A sample of about 2–4 mg was loaded into the alumina crucible and heated (10˚C/min) in an O_2 atmosphere to 900˚C. Catalyst morphologies were analyzed using high-resolution transmission electron microscopy (JEOL-2100) operating at 200 kV. X-ray photoelectron spectroscopy (XPS) was performed on fresh and spent catalysts to detect the chemical state of elements using AXIS SUPRA with Al Kα radiation ($h\nu = 1486.69$ eV). The binding energy at 284.8 eV corresponding to carbon 1*s* was chosen as the reference for the binding energy calibration of all elements present in the catalyst.

2.5. Catalytic reaction studies

2.5.1. Experimental setup

Methane reforming studies were carried out in a fixed bed reactor consisting of a quartz tube with i.d.= 8 mm, o.d. = 12 mm, and length = 540 mm. A furnace with three heating zones (Applied Test Systems, 3210) along the quartz tube's axial length was used to heat the reactor. The zone temperatures were controlled and monitored by an electronic temperature controller (Waltow) and K-type thermocouples. Mass flow controllers (0–200 ml/min, Bronkhorst EL-Flow) were used to regulate the flow of gases. Steam was produced by supplying required quantities of H_2O using calibrated HPLC pump (0.01–10 ml/min, LabAlliance Series I) through the pre-heater zone maintained at 250°C. Products were allowed to cool down in a condenser held at 1°C using a chiller (Zulabo F25), followed by condensing the steam in a gas-liquid separator (GLS). Dry gases were analyzed for composition using gas chromatography (GC-2014, Shimadzu Corporation) equipped with a thermal conductivity detector (TCD) and carboxane-packed column.

2.5.2. Parametric study and experimental procedure

Kinetic studies were performed by changing feed composition, temperature, and weight hourly space velocity (WHSV). The calcined sample was mixed with quartz beads and placed in a quartz tube with the support of quartz wool. The mass of quartz beads used throughout the experiments was kept constant at 250 mg and this corresponds to dilution ratio of 10 (quartz beads:catalyst) for 25 mg of loading. Before loading, the quartz beads were treated in HNO_3 followed by calcination at 900°C to remove any impurities. The CH_4/CO_2 ratio was maintained at 2 for all reactions, except for SRM. Consequently, the variation in the feed compositions is the result of altering the flow rates of N_2, H_2O, and O_2 as presented in Table 3.

To maintain the total flow ≈ 140 ml/min on a dry basis in SRM and CDSRM, the flow rate of N_2 was increased to 90 ml/min in SRM to maintain same residence time in both cases. In the case of TRM, the choice of S/C and O/C on the catalytic studies were limited to 0.88, 1.17, and 0.1, 0.2 respectively, as any other higher parametric combinations have affected X_{CO_2} negatively (cf. Fig. S4). The effect of temperature was studied in the range of 600–800°C with a 50°C step change. Effect of catalyst loading was studied in terms of WHSV ($\dot{V}_{feed}/m_{cat}\ m^3\ hr^{-1}\ kg^{-1}$). Specifically, 25 mg, 50 mg, and 100 mg loadings were used for which the WSHVs can be approximated to 336, 168, and 84, respectively, on a dry and O_2-free basis. Before conducting the reactions, in order to study the effect of reduction time, the calcined catalyst was reduced in situ in 40 vol% H_2/N_2 mixture at 800°C for 2, 3, and 4 h. Based on the obtained results as explained in the sections to follow, the reduction time was set for the other catalytic studies. Through an online gas chromatograph, product gases on a dry basis were analyzed every for 13 min, and the conversions and syngas molar ratio were calculated using molar flow rates ($\dot{F}_k$ mol/s) according to

$$X_k = \frac{\dot{F}_k^{in} - \dot{F}_k^{out}}{\dot{F}_k^{in}}, \quad \frac{n_{H_2}}{n_{CO}} = \frac{\dot{F}_{H2}^{out}}{\dot{F}_{CO}^{out}}.$$

Table 3
Feed compositions used for experimental investigations.

Feed molar ratios	Feed flow rates (sccm)					
(CH_4/CO_2, S/C, O/C)	N_2	CH_4	CO_2	H_2O	O_2	Total
DRM						
(2, 0, 0)	70	46.66	23.33	0.0	0.0	140
SRM						
(0, 0.88, 0)	90	46.66	0.0	41.27	0.0	177.93
(0, 1.17, 0)	90	46.66	0.0	55.03	0.0	191.69
(0, 1.47, 0)	90	46.66	0.0	68.79	0.0	205.45
(0, 1.77, 0)	90	46.66	0.0	82.55	0.0	219.21
CSDRM						
(2, 0.88, 0)	70	46.66	23.33	41.27	0.0	181.26
(2, 1.17, 0)	70	46.66	23.33	55.03	0.0	195.02
(2, 1.47, 0)	70	46.66	23.33	68.79	0.0	208.78
(2, 1.77, 0)	70	46.66	23.33	82.55	0.0	222.54
TRM						
(2, 0.88, 0.1)	70	46.66	23.33	41.27	4.7	185.96
(2, 0.88, 0.2)	70	46.66	23.33	41.27	9.4	190.66
(2, 1.17, 0.1)	70	46.66	23.33	55.03	4.7	199.72
(2, 1.17, 0.2)	70	46.66	23.33	55.03	9.4	204.42

3. Results and discussion

3.1. Pre-reaction sample characterization

3.1.1. Structural and morphological properties

Powder XRD patterns of calcined catalyst and its reduced phases at different reduction times are shown in Fig. 1.

For phase structure identification, corresponding powder diffraction file (PDF) card numbers are indicated with their respective diffraction patterns. Peak broadening of reflections is observed for all the facets indicative of finite average crystal size. For calcined catalyst at 800°C, reflections are observed at $2\theta = 31.80$, 37.34, 45.54, 60.38, and 66.41, characteristic of both $NiAl_2O_4$ and γ-Al_2O_3.

All these observed reflections are shifted to lower Bragg angles w.r.t the facets of γ-Al_2O_3 (PDF: 56–0457). From Bragg's law, the downward shift of Bragg angle is due to the substitution (doping) of larger ionic radii of Ni^{2+} cation (83 pm) into the γ-Al_2O_3 crystal lattice with lower ionic radii of Al^{3+} cation (67.5 pm) [43]. Apart from creating a micro-strain in the crystal lattice, the doping results in an inactive nickel aluminate ($NiAl_2O_4$) phase. For the calcined sample since the major NiO reflection at $2\theta = 43.27$ is not observed, we conclude that the reflection at $2\theta = 37.24$ is also not due to NiO. Furthermore, the minor reflection at $2\theta = 62.87$ is also not observed. The absence of NiO patterns in the calcined sample is either due to the doping of Ni into the γ-Al_2O_3 lattice or due to the high dispersion of NiO on the surface. The formation of $NiAl_2O_4$ phase depends on high calcination temperatures in excess of 700–750°C [44,45], while the detectable NiO phase in the calcined samples depends upon initial stoichiometry of Ni and Al, calcination temperature, and the preparation methods [46–48,45]. The calcination temperature and the sub-saturation stoichiometry of initial precursors used in the catalyst preparation resulted in an experimentally observed lattice parameter of 7.979 Å, which is close to stoichiometric nickel aluminate (8.048 Å) confirming that the calcined catalyst is also composed of spinel structure [43].

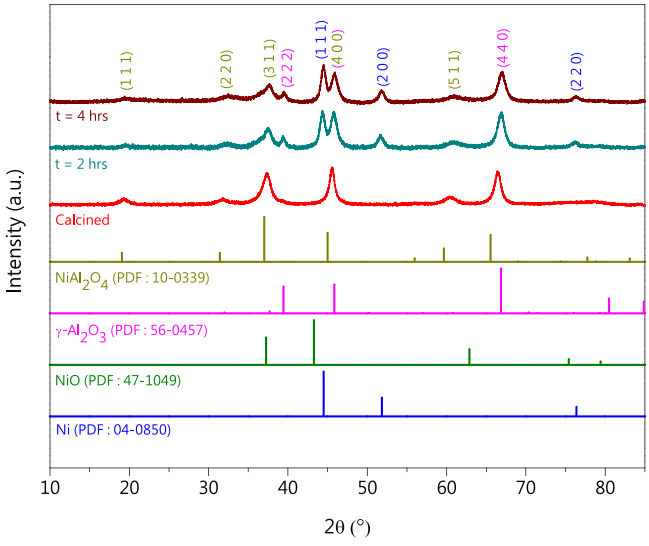

Fig. 1. XRD pattern of as calcined and reduced catalysts. Reduction Conditions: 40 vol% H_2/N_2 at 800 °C for 2hrs, 3hrs, and 4hrs.

Reduction aided the Ni to exsolve from the lattice resulting in visible characteristic reflections at $2\theta = 44.50$, 51.84, and 76.36. Further interpretation of this observation can be augmented by the relative reflection shift of all the facets of reduced catalysts to higher Bragg angles w.r.t calcined catalysts. Consequently, the experimentally observed lattice parameters for 4 h and 2 h reduced samples are 7.905 Å and 7.917 Å respectively which are in close agreement with γ-Al_2O_3 (7.911 Å). Though a difference between the reduced samples at $t = 2$, and 4 h is unnoticeable, the calculated intensity ratios (I_1, I_2) of Ni(111), $NiAl_2O_4$(311), and γ-Al_2O_3(440) facets relate the obvious differences as represented in Table 4. An increase in I_1 suggests that the bulk support is progressively enriched with alumina, while from I_2 it can be interpreted that the Ni exsolve from the spinel structure in the H_2 environment.

3.1.2. Vibrational spectroscopy

Surface characterization of the calcined and reduced catalysts is performed using infrared spectroscopy, and the corresponding transmission spectrum is represented in Fig. 2. The broad FTIR peaks around 3446 cm^{-1} and 1638 cm^{-1} corresponds to surface hydroxyl group and adsorbed water peaks. [49]. The group of peaks in the range of 2960–2852 cm^{-1} is indicative of the C-H bond from the carbonaceous residues linked to the usage of citric acid and ethylene glycol [49,50] while the spectra at ≈ 1386 cm^{-1} corresponds to carbonates. Structural properties of γ-Al_2O_3 closely resemble that of spinel, yielding both tetrahedral (Al^{3+}_{Tetra}) and octahedral (Al^{3+}_{Octa}) coordinate sites, while in NiO, Ni atoms are always octahedrally (Ni^{2+}_{Octa}) coordinated. Due to the presence of Al^{3+} ion vacancies (≈ one-third) in γ-Al_2O_3, Ni^{2+} diffusion into the lattice results in tetrahedral (Ni^{2+}_{Tetra}) and Ni^{2+}_{Octa} coordinated sites [51]. Accordingly, the resulting spinel structures can be identified in the IR spectra below 1000 cm^{-1}.

Metal-oxygen bond (M-O) in the frequency range 400–450 cm^{-1} results in octahedral species, but the tetrahedral stretching bands are observed in the range of 500–900 cm^{-1}. Characteristic of the latter bands are Al-O, M-O, and M-O-Al bonds with two types of Al-O coordination sites (AlO_6 and AlO_4). From Fig. 2 the frequency spectra at ≈ 721 cm^{-1} is distinctive vibration of tetrahedrally coordinated Al-O bond (or Ni^{2+}_{Octa}) and the peak at ≈ 532 cm^{-1} is the Al-O bond coordinated octahedrally (or Ni^{2+}_{Tetra}) [52–54]. The presence of these two broad bands confirms the formation of nickel aluminates. Additional vibrational modes at ≈ 1157 cm^{-1} and ≈ 1087 cm^{-1} are attributed to δ_{as}Al-O-H and δ_sAl-O-H, respectively with well-defined peaks in reduced samples indicating the formation of alumina [50,55].

3.1.3. Reduction studies

Identification of reducible Ni species is performed using H_2-TPR and as indicated in Fig. 3, the H_2 consumption shows a broad peak at 798°C.

To further identify the species contributing to such a large reducing temperature, nickel coordination needs to be understood. As explained earlier, the γ phase of alumina has both Al^{3+}_{Tetra} and Al^{3+}_{Octa} sites [51]. In the presence of Ni, these coordination sites result in normal spinel $Ni^{2+}[Al^{3+}_2]O_4$ and the inverse spinel $Al^{3+}[Ni^{+2}Al^{3+}]O_4$ which are designated as Ni^{2+}_{Tetra} and Ni^{2+}_{Octa} respectively [56]. The evolution of these two species depends on the metal loading and calcination temperature. It is known that Ni^{2+} prefers Ni^{2+}_{Octa} sites, but with increasing the calcination temperature, the Ni^{2+} diffuses from Ni^{2+}_{Octa} to Ni^{2+}_{Tetra} sites. Wu et al. [57] studied the effect of reduction time and calcination temperatures of nickel aluminates and termed the Ni^{2+}_{Tetra} as "hard to reduce" and Ni^{2+}_{Octa} as "readily reduced" sites. Accordingly, the observed broad reduction peak at 798 °C in this work can be assigned to the Ni^{2+}_{Tetra} species, which can be narrowed down to the temperature range of 750–950 °C [58]. A similar reduction profile was observed in previous works from our group when a commercial γ-Al_2O_3 was used as support for 15 wt% Ni [59,60].

Table 4
XRD intensity ratios of calcined and reduced samples.

Sample	$I_1 = I_{(440)}/I_{(311)}$	$I_2 = I_{(111)}/I_{(311)}$
Calcined	1.10	0.0
t_{red} = 2 hrs	2.22	2.53
t_{red} = 4 hrs	2.48	3.57

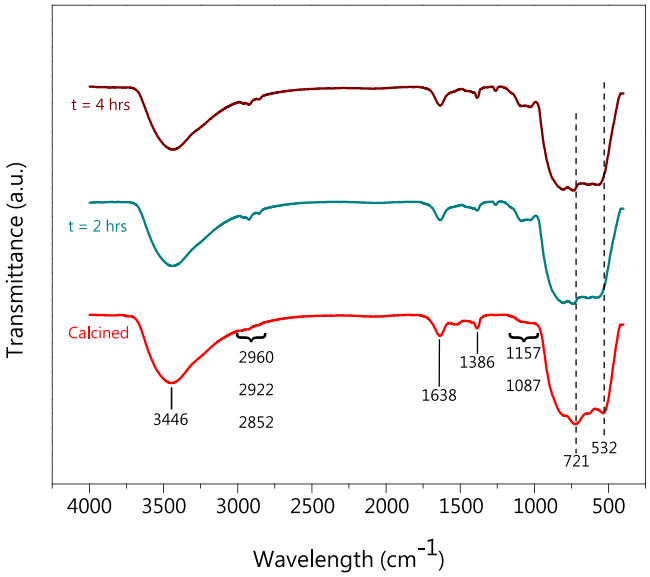

Fig. 2. FTIR spectra of calcined and reduced catalysts.

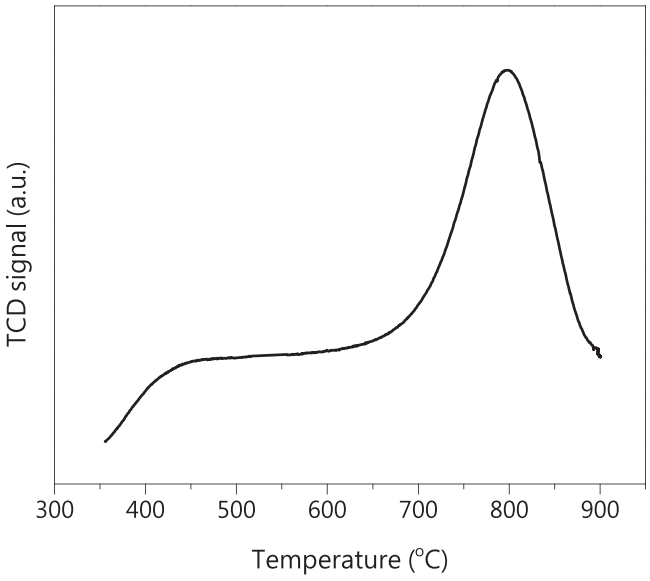

Fig. 3. H_2-TPR of calcined catalyst at 800°C.

3.1.4. Nitrogen physisorption studies

Porous material characteristics such as specific surface area, mean pore diameter, and pore volume determine the metal dispersion on the support. Accordingly, from the N_2 adsorption-desorption studies, these textural properties are calculated and reported in Table 5.

All the isotherms, presented in Fig. S7 exhibit type IV isotherms with a well-defined H3 hysteresis loop, indicating a very wide pore distribution of the catalyst (cf. Fig. S8). These observations are in agreement with work on the synthesis of silica using the sol-gel method with base catalysis (NH_4OH) by Ro et al. [61]. Compared to the as-prepared calcined sample, the BET surface area of the reduced samples

Table 5
Textural properties.

Sample	Area (m^2/g)			Volume (cm^3/g)		μ_{dia} (nm)†
	BET	Micropore	External	Total	Micropore	
Calcined	103.4	–	103.97	0.1321	–	5.62
Reduced (2 h)	87.56	–	87.27	0.1419	–	6.84
Reduced (4 h)	58.23	10.13	48.11	0.1437	0.00485	10.19

† Average pore diameter (nm) calculated using BJH method.

decreases with an increase in reduction time. However, the corresponding changes in the total pore volume obtained from the BJH method are insignificant. External surface area, a combination of mesopores and macropores, also follows the same trend as that of BET, and this can be attributed to the pore blockage by the nickel coming out of the $NiAl_2O_4$ crystal lattice, which has been confirmed by the XRD. Pore size distribution (PSD) curves, shown in Fig. S8 are calculated using the adsorption isotherm and for the 4 h reduced catalyst, a wide pore volume distribution was observed in the range of 3–6 nm in comparison to the others.

3.1.5. Chemical oxidation studies

To study the chemical nature of the elements on the catalyst surface, XPS analysis of the calcined and reduced catalysts is performed and the results are shown in Fig. 4. The Ni 2p scan has two main peaks Ni $2p_{3/2}$, Ni $2p_{1/2}$, and their respective satellite peaks. The splitting of the main peaks is due to the spin-orbital coupling of the angular momentum vector and the electron spin, while the presence of satellite peaks is due to the 4 s-3d orbitals interaction resulting in different occupations of 3d orbitals. Accordingly, the Ni^{2+} $2p_{3/2}$ spectrum lies in between pure NiO ($\approx$ 854.4 eV) and $NiAl_2O_4$ ($\approx$ 857.3 eV) [62,63]. This $2p_{3/2}$ spectrum is centered around $\approx$ 856.0 eV with a satellite peak having $\approx$ 6.3 eV binding energy (BE) above the main peak. Accordingly, for the as-prepared catalyst, doublets with average BEs of $\approx$ 855.95 eV and $\approx$ 874.42 eV are observed. These characteristic Ni^{2+} peaks with BE around $\approx$ 857.42 eV is due to nickel in octahedral positions while the $\approx$ 856.29 eV BE is associated with nickel occupying the tetrahedral positions [46]. Moreover, a satellite peak with a separation of $\approx$ 6.0 $\pm$ 3.0 eV further confirms the Ni^{2+} oxidation state. As for the reduced catalysts, the BE of the octahedrally coordinated nickel increased to higher values which could be due to different levels of MSI in the inverse spinel. No peaks relating to the BE of NiO species are observed, indicating that nickel is well dispersed on the support and exhibits a strong metal-support interaction, in agreement with XRD. Further, from the XPS of the reduced samples, it can be inferred that nickel occupying octahedral positions is easy to reduce than the tetrahedral ones.

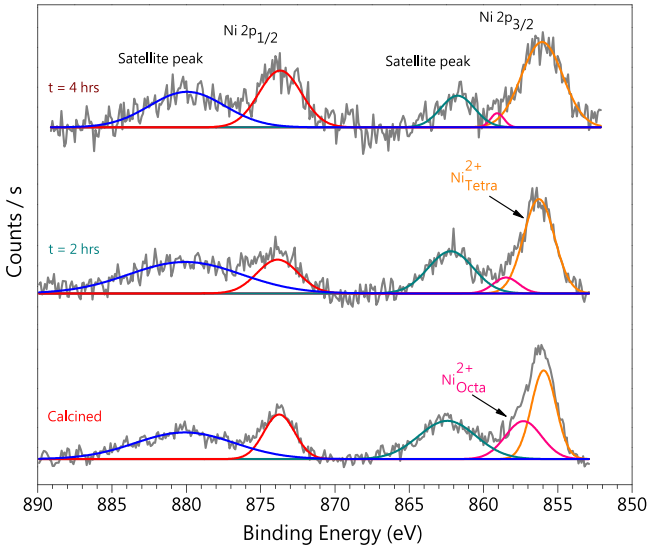

Fig. 4. XPS of calcined and reduced catalysts.

3.2. Catalytic reforming studies

3.2.1. Optimum process conditions

Identification of process conditions is important in designing the experiments to achieve maximum per-pass conversion. Residence time is one such variable that significantly affects conversion. For heterogeneous reactions, the residence time can be quantified in terms of weight hourly space velocity (WHSV, $m^3\ hr^{-1}\ kg^{-1}$), defined as the feed volumetric flow rate per mass of the catalyst. WHSV can be adjusted to achieve reaction conditions that are near or away from equilibrium conditions. For a feed flow rate of $\approx$ 140 ml/min (dry and O_2-free basis), three different catalyst loadings (25 mg, 50 mg, and 100 mg) are chosen to obtain WHSV of 336, 168, and 84 respectively. To identify the optimum residence time out of these, experiments for all the CSDRM conditions presented in Table 3 are performed. The experiments are performed at 800°C using the catalyst reduced for 2 h at 800°C. The observed conversions are also compared to equilibrium predictions.

The time-on-stream data at WHSV = 84 for four different S/C ratios is shown in Fig. 5. For each S/C, the experiments are conducted for 3 h. At the specified conditions catalyst showed a stable catalytic activity, and the obtained X_{CH_4}, X_{CO_2}, and H_2/CO ratio are close to chemical equilibrium. A close observation of the effect of S/C on the process variables shows that by increasing the steam content, X_{CH_4} increases while X_{CO_2} decreases· H_2O and CO_2 compete for the same active sites of the support during CSDRM, resulting in the observed inverse dependence of the S/C on X_{CO_2} [64]. Guilhaume et al. studied the competitive adsorption of H_2O and CO_2 on 10%Ni-0.05%Rh/$MgAl_2O_4$ at T = 25–500°C and reported that the total adsorbed H_2O was always 3 times higher than that of CO_2 [65]. The obtained individual adsorption isotherms were fitted for a Temkin-based model to predict the coverages at T = 600–800°C relevant to the CSDRM conditions. The Temkin-based model predicted that the CO_2 adsorbed dissociatively till 500°C, after which the surface coverage of the species related to CO_2 decreased much faster than that of H_2O [65]. With the increase in steam content, the production of H_2 from the SRM increases, which explains the observed increase in X_{CH_4} and H_2/CO. Similar conclusions were drawn by Singh et al. for CSDRM at CH_4/CO_2 = 3 and varying S/C (0.33, 0.44, and 0.66)

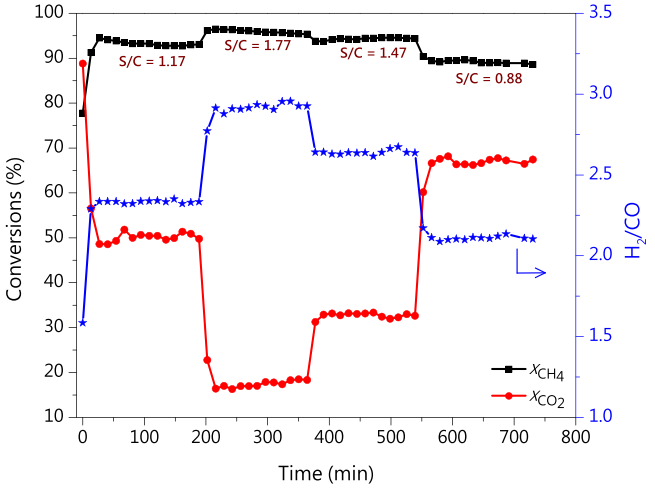

Fig. 5. Time on stream conversion of CH_4 (X_{CH_4}) and CO_2 (X_{CO_2}), and H_2/CO ratio for combined steam and dry reforming (CSDRM). Experimental conditions: CH_4/CO_2 = 2, S/C = 0.88–1.77, T = 800°C, t_{red} = 2 hrs, WHSV = 84 $m^3\ hr^{-1}\ kg^{-1}$.

on 10 wt% Ni/SBA-15 catalyst at 800°C [66]. Although not shown here, WHSV of 168 $m^3\ hr^{-1}\ kg^{-1}$ also resulted in a stable catalytic activity with compositions close to equilibrium. For WHSV of 336 $m^3\ hr^{-1}\ kg^{-1}$, a S/C = 0.88 resulted in X_{CH_4} = 58.65%, X_{CO_2} = 41.61%, and H_2/CO = 2.26, which is away from equilibrium conditions (Fig. S9). The discussion on experimental investigations of S/C = 1.17, 1.47, and 1.77 is reserved for the following sections. In general, with the increase in WHSV (from 84 to 336), conversions (X_{CH_4}, X_{CO_2}) decreased and H_2/CO increased. Since the conversions for WHSV = 86 and 168 are close to equilibrium, they are not used for further investigations, and WHSV = 336 $m^3\ hr^{-1}\ kg^{-1}$ is considered to further study the effect of feed compositions, reduction time (t_{red}), and operating temperature.

The effect of reduction time of the catalytic activity is studied by considering the catalysts reduced for different times (t_{red} = 2, 3, and 4 h). A systematic study of the effect of reduction time on the catalytic activity requires the measurement of kinetic data away from equilibrium. This ensures that a meaningful correlation can be drawn between catalyst structural, chemical, and morphological changes that transpired due to the reduction time and the observed kinetic data. Accordingly, the CSDRM with process conditions of WHSV = 336 $m^3\ hr^{-1}\ kg^{-1}$, T = 800°C, and S/C = 0.88 is performed at different t_{red} and the results are reported in Table 6. With the increase in t_{red} to 3 h the conversions (X_{CH_4}, X_{CO_2}) increased by ≈ 10%, however, the H_2/CO remained constant. A further increase in t_{red} to 4 h has not resulted in any further improvement in conversion.

The substantial change in conversions w.r.t t_{red} is due to the improved free nickel surface sites. As shown in XRD, the incremental change in peak intensities of the Ni(111) facet from 2 h to 4 h resulted in an I_2 of 2.53 and 3.57 respectively, indicating that surface nickel availability exsolved from the $NiAl_2O_4$ has increased due to the prolonged reduction. From H_2-TPR studies, it is inferred that the Ni^{2+}_{Tetra} sites accounted for the high reduction temperature and are "hard to reduce" [57,58]. Analogously from the XPS studies with an increase in t_{red} the intensities corresponding to Ni^{2+}_{Tetra} sites decreased while the corresponding I_2 from XRD (cf. Table 4) increased. This explains the positive effect of longer reduction time on the availability of free surface nickel sites and the subsequent increase in observed conversions. So, throughout this study a t_{red} = 4 hrs and WHSV = 336 $m^3\ hr^{-1}\ kg^{-1}$ is used.

3.2.2. Dry reforming of biogas

Biogas, without any purification when reformed at elevated temperatures, produces syngas due to DRM. Thus to establish a base case for the reforming of biogas, DRM is conducted, and the results are shown in Fig. 6.

Since CO_2 is the limiting reactant, X_{CO_2} is greater than X_{CH_4}, and the H_2/CO ratio is slightly greater than unity. Similar studies on the effect of biogas feed compositions performed by Karemore et al. [67] and Pawar et al. [59] resulted in a X_{CH_4} ≈ 47.3–48.5%, X_{CO_2} ≈ 79–91.7%, and H_2/CO = 1.12. The low CH_4 conversion reported here is due to the high WHSV = 336 employed in comparison to the WHSV = 4 by Karemore et al. [67] and 16.2 by Pawar et al. [59]. Reforming of biogas in excess of CH_4 (i.e., $CH_4/CO_2 > 1$) causes coke deposition and results in a gradual decrease in conversions on time on stream. Such a drop in conversions is observed by Pawar et al. [68]; however, not observed here. This could be due to the formation of well-dispersed nickel as a result of strong MSI, as confirmed by fresh catalyst's XRD, TPR, XPS, and FTIR characterizations.

Table 6
Effect of t_{red} on CSDRM.

t_{red} (hrs)	X_{CH_4}	X_{CO_2}	H_2/CO
2	57.88 ± 1.2	41.52 ± 1.8	2.27 ± 0.05
3	69.23	49.67	2.28
4	65.51 ± 4.3	50.44 ± 2.2	2.16 ± 0.11

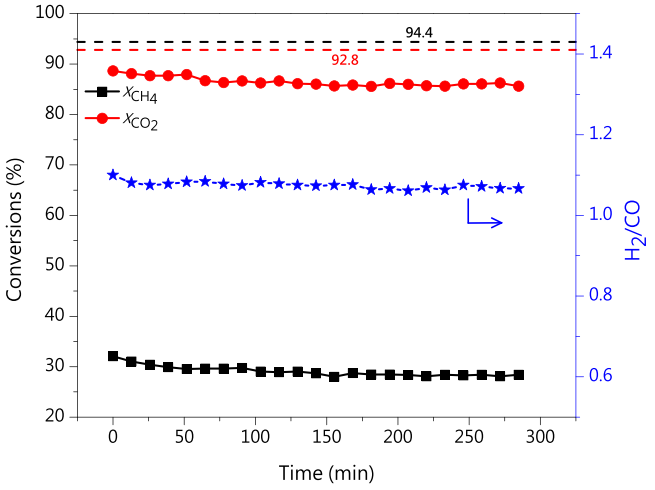

Fig. 6. Time on stream conversion of CH_4 (X_{CH_4}) and CO_2 (X_{CO_2}), and H_2/CO ratio for dry reforming. Experimental conditions: CH_4/CO_2 = 2, T = 800°C, t_{red} = 4 hrs, WHSV = 336 $m^3\ hr^{-1}\ kg^{-1}$ (Dashed lines represents equilibrium conversions).

3.2.3. Combined steam and dry reforming of methane

The effect of H_2O on dry reforming of biogas is studied in the temperature range of 600–800°C with the inlet feed conditions presented in Table 3. The effect of temperature at a particular S/C is studied by starting the reaction at 800°C and gradually decreasing the temperature to 600°C in a step of ΔT = 50°C. The experimental observations are presented in Figs. 7, 8, S10, and S11. The conversions, exit mole fractions, and H_2/CO are represented in Figs. 7(a), (b), and S10 respectively and for comparison purpose, the equilibrium predicted values are also reported in the respective graphs. Fig. 7(e) shows a high initial X_{CH_4} in the range of 75–87% at 800°C, however, the conversions decrease rapidly over a period of 3 h. The rate of fall in X_{CH_4} for this period is 20.94%, 12.74%, 11.0%, and 18.97% for all four S/C ratios in the increasing order. This implies that the rate of deactivation depends on S/C, and for the cases presented here, the minimum deactivation rate is observed at S/C = 1.47. The initial catalyst deactivation was also observed by Prasad et al. during the SRM on Ni-CGO and Ni-CZO catalysts [26,27]. Among the conditions they reported, steam-rich conditions (S/C = 1.0, 1.5, 2.0) have shown high catalyst deactivation while the steam-lean condition (S/C = 0.5) showed moderate deactivation [27]. It is to be noted that the same catalyst under the same operating conditions, however, at lower WHSV = 84 $m^3\ hr^{-1}\ kg^{-1}$, showed a stable catalytic activity (cf. Fig. 5). This establishes a strong relationship between catalyst deactivation and WHSV, as operating at lower WHSV resulted in stable and close to equilibrium compositions. At low WHSV the catalyst loading is high and therefore, there are enough active catalyst sites to convert the gas volume even if a fraction of the active sites become deactivated. However, at high WHSV, the catalyst loading is low and therefore, a large fraction of active sites becomes deactivated.

To further examine the effect of residence time, using a WHSV = 168 $m^3\ hr^{-1}\ kg^{-1}$ the CSDRM was performed at 800°C for all four S/C ratios with a t_{red} = 2 h and 4 h. Irrespective of S/C and t_{red}, the catalyst showed stable catalytic activity close to equilibrium (not shown). From the WHSV and the temperature studies, we can infer that deactivation is a function of residence time (WHSV) and a high-temperature phenomenon as there is no transient behavior at lower temperatures and WHSV (cf. Figs. 5, 7(e)). From Fig. 7(f) it can be seen that the catalyst deactivation resulting in the drop of X_{CH_4} is not observed in case of X_{CO_2}. This is because oxidizer (CO_2, H_2O) and CH_4 activation happens on different sites as Ni enhances the CH_4 dehydrogenation while the support participates in the adsorption of CO_2 and H_2O. The other findings from the CSDRM studies are

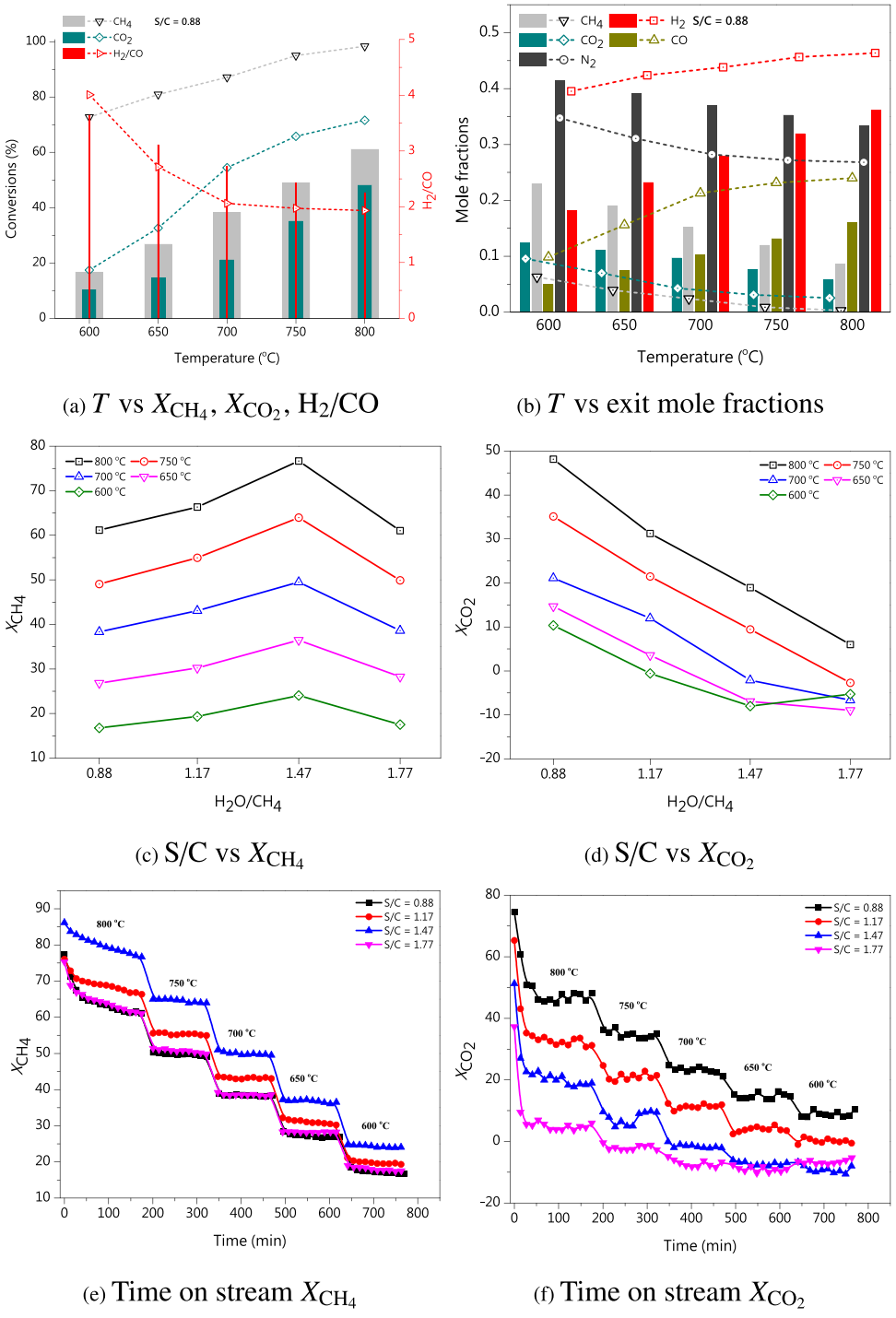

Fig. 7. Conversions, exit mole fractions and H_2/CO for Combined steam and dry reforming. Experimental conditions: $CH_4/CO_2 = 2$, $T = 800–600$°C, $t_{red} = 4$ hrs, WHSV $= 336\ m^3\ hr^{-1}\ kg^{-1}$, (a) & (b) S/C = 0.88, (c)-(f) S/C = 0.88–1.77, (a) & (b) Comparison with equilibrium predictions (dashed lines with points represent equilibrium values).

- X_{CH_4} increases with an increase in S/C ratio till S/C = 1.47 and drops afterwards as shown in Fig. 7(c), which is due to catalyst deactivation at high S/C.
- X_{CH_4} and X_{CO_2} increases with an increase in T as both SRM and DRM are endothermic.
- X_{CO_2} decreases with an increase in S/C ratio (cf. Fig. 7(d)) as more content of steam enhances the less energetic SRM and also WGSR. In particular, for certain combinations of reaction temperature and high S/C (≥ 1.17) ratios, as shown in Fig. 7(d) CO_2 is produced due to the occurrence of WGSR.
- H_2 production follows that of CH_4 consumption as shown in Fig. S11 (c). While the CO mole fraction decreases with an increase in S/C ratio (cf. Fig. S11(d)) as the steam presence in higher quantities suppresses the adsorption of CO_2 and also enhances the WGSR.
- H_2/CO molar ratio decreases with an increase in T as shown in Fig. 8 because of the increase in CO production due to enhanced kinetics of DRM (cf. Fig. S11(d)) and the RWGS. While the H_2/CO molar ratio increased with the increase in the S/C ratio due to the kinetically favorable SRM producing 3 moles of H_2 per mole of CH_4 as well as the consumption of CO due to WGSR.

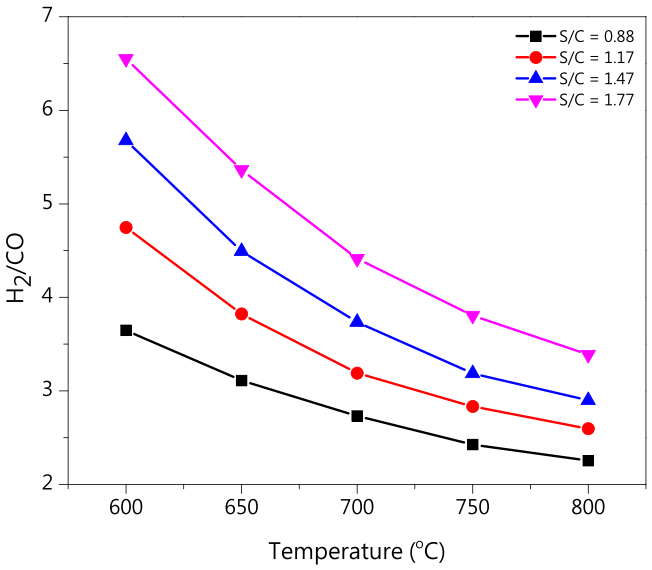

Fig. 8. H_2/CO at different S/C for combined steam and dry reforming. Experimental conditions: $CH_4/CO_2 = 2$, S/C = 0.88–1.77, $T = 800$–600°C, $t_{red} = 4$ hrs, WHSV = 336 $m^3\ hr^{-1}\ kg^{-1}$.

Through the CSDRM route, a stable $H_2/CO = 2.16 \pm 0.11$ is achieved with a corresponding $X_{CH_4} = 65.51 \pm 4.3\%$ and $X_{CO_2} = 50.44 \pm 2.2\%$ at S/C = 0.88. The catalyst deactivation observed at a lower residence time (high WHSV) is addressed by increasing the catalyst loading (low WHSV), thus increasing the residence time.

This positive effect of low WHSV (or GHSV) on the catalyst stability depends upon the catalyst's size, catalyst composition, and rate of methane decomposition [25,69]. Zhai et al. studied the effect of GSHV on the catalyst stability of different Ni-based catalysts for SRM (S/C = 3) [25]. Among the studied catalyst, $Ni_{0.5}Mg_{2.5}AlO_9$ showed stable activity for 150 hrs at low GHSVs ($6 \times 10^4\ hr^{-1}$, $1.85 \times 10^5\ hr^{-1}$), but with an increase in GHSV to $6 \times 10^5\ hr^{-1}$ deactivation was observed due to spinel formation. To further study the occurrence of other deactivation routes, $Ni/ZrO_2/Al_2O_3$ catalyst which was reported to be unstable even at low GSHV ($8 \times 10^4\ hr^{-1}$), was tested for Ni re-oxidation by repeated cycles of reaction and reduction in H_2 environment. This resulted in the conclusion that the catalyst deactivation was not associated with Ni re-oxidation, but due to sintering and carbon deposition [25]. Similar studies on the effect of GSHV and the effect of Ni particle size on the catalyst stability were conducted by Hou et al. for the oxidative reforming of CH_4 and CO_2 (CH_4:CO_2:O_2 = 10:4:3) [69]. The results indicate that catalysts with average Ni particle size (< 16 nm) showed high catalyst stability. Interestingly, the catalyst Ni (4.5 nm), which was stable for GHSV of $9 \times 10^3\ hr^{-1}$, $18 \times 10^3\ hr^{-1}$, and $54 \times 10^3\ hr^{-1}$ for 80 hrs was inactive for a GHSV of $9 \times 10^4\ hr^{-1}$. Above a certain GHSV, the relative rate of CH_4 decomposition will be lower than the oxidative removal of surface carbon which leads to a decrease in CH_4 conversion and eventually the Ni re-oxidation by O_2. While the effect of particle size on the catalyst stability is due to the low rate of methane decomposition on the larger particles (45 nm) when compared to smaller ones (4.5 nm). This essentially imbalances the rate of methane decomposition and oxidative removal of surface carbon, thus exposing the Ni to the O_2 environment to oxidize to NiO [69]. In the present study on CSDRM, the catalyst deactivation at high GSHV (or WHSV) could be due to the relatively low rate of decomposition of CH_4 when compared to the high surface hydroxyl formation, which eventually leads to the migration of active nickel on the surface resulting in the sintering of the active metal [28–30]. Nevertheless, it should be noticed that we have performed the deactivation studies only for short time on streams.

3.2.4. Steam reforming of biogas

From the kinetic studies of CSDRM, it is evident that the use of high steam content results in catalyst deactivation. To further investigate the effect of steam on catalyst deactivation, SRM was conducted under the same operating conditions. The only change is in the flow rate; 136.66 ml/min on a dry basis for SRM as opposed to 140 ml/min for CSDRM as given in Table 3. This resulted in a slightly lower WHSV = 328 $m^3\ hr^{-1}\ kg^{-1}$. It is to be noted that the reported WHSV in the current work is on a dry and O_2-free basis.

To conduct the SRM, the same procedure as that of CSDRM is followed, and the obtained results are shown in Fig. 9 and Figs. S12, and S13. Similar to the CSDRM, the initial catalytic activity is high in SRM, and a gradual decrease in X_{CH_4} is observed. As shown in Fig. 9(a) the deactivation rate for the S/C = 1.17 is low and the associated initial deactivation rates for increasing order of S/C ratios are 12.43%, 2.17%, 5.71%, and 24.49% respectively. Except for the S/C = 1.77, these calculated deactivation rates are lower than their CSDRM counterparts, suggesting that both H_2O and CO_2 contribute to catalytic activity loss. Unlike the CSDRM, a close to steady state operation is achieved for S/C = 1.17, probably due to stoichiometric feed conditions, and the observed results are in agreement with the equilibrium predictions as shown in Figs. S12(a) and S12(b). An increase in the S/C ratio from 1.47 to 1.77 reduced the initial catalytic activity by ≈ 19.0%. The steam-assisted transformation of surface nickel to aluminates and nickel sintering in high steam environments explains the observed deactivation [28,29]. The active sites for SRM is the metallic nickel rather than the unreduced spinel [70]. Apart from these, the other major findings from the steam reforming study are as follows

- X_{CH_4}, H_2, and CO mole fractions trends are in agreement with CSDRM w.r.t S/C ratios and T (cf. Fig. S13(b), S13(c)).
- X_{CH_4} in SRM is slightly lower when compared to the same operating conditions in CSDRM.
- H_2/CO ratio for the same operating conditions is always higher than the ones observed in CSDRM due to the absence of CO_2 resulting in a lower CO mole fraction in SRM (cf. Fig. S13(c)).
- The production of CO_2 increased with increasing S/C ratio during SRM due to WGSR, as represented in Fig. S13(d). As the WGSR is slightly exothermic maximum production of CO_2 is observed at 650 °C.

3.2.5. Tri-reforming of biogas

The TRM reaction is carried out for a synthetic biogas composition of 66.67% CH_4, 33.33% CO_2, and for varying S/C and O/C ratios as represented in Table 3. The four model TRM compositions are tested individually, and the results are shown in Figs. 10, and S14. The experimental observations are all well within the limit predicted by thermodynamic equilibrium, which is indicated by dashed lines in Figs. 10(a)-(d) and S14(a)-S14(d). In TRM, achieving an optimum X_{CO_2} with a desired H_2/CO ratio requires a proper selection of initial feed compositions and an appropriate operating temperature range as both (X_{CO_2}, H_2/CO) have an inverse relationship. From Fig. S5, it is clear that a S/C = 0.88 is required to maintain $H_2/CO \approx 2$. Based on the thermodynamic analysis, to limit the negative impact of S/C and O/C on X_{CO_2}, in this study, their maximum values are set to 1.17 and 0.2, respectively.

The CSDRM with S/C = 0.88 and 1.17 has shown initial deactivation behavior, but with the addition of O_2, the catalyst stability is improved, as shown in Figs. 10(e), 10(f), S14(e), and S14(f). It should be noticed that the reactions are performed only for a short duration of 600 min and therefore, the stability here refers to short term stability. Due to the improved catalyst stability, the exit CO_2 mole fractions reached equilibrium conditions especially with O/C = 0.2 at all temperatures (cf. Figs. 10(c), S14(c)). Among the test conditions, the highest X_{CO_2}(=55.13%) is observed at $T = 800$°C, S/C = 0.88, and O/C = 0.1 as shown in Fig. 10(e). According to Luneau et al. $NiAl_2O_4$ and 5 wt%Ni/

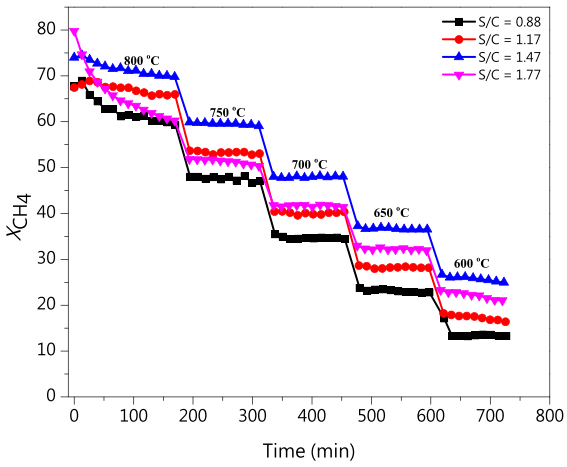

(a) Time vs X_{CH_4}

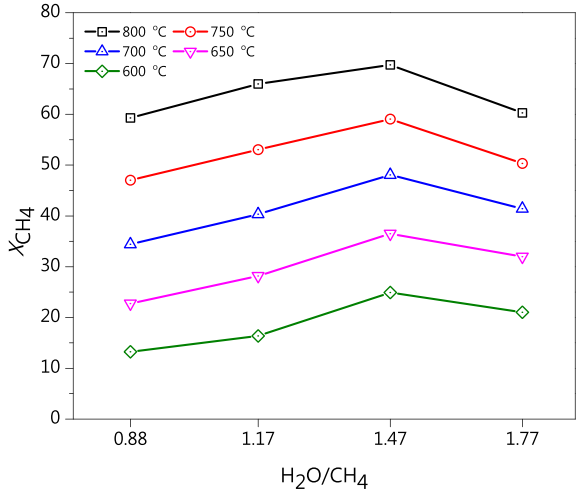

(b) S/C vs X_{CH_4}

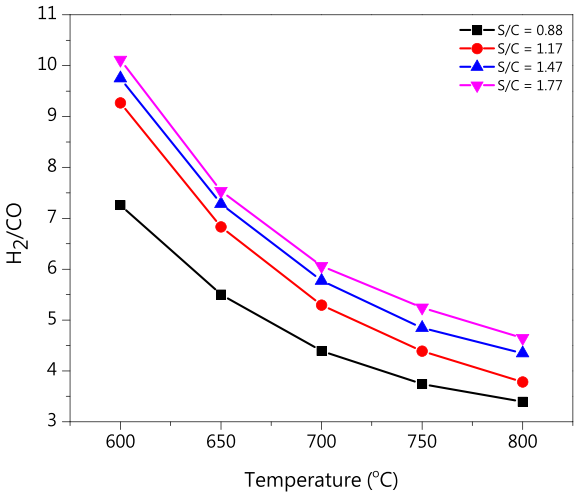

(c) T vs H_2/CO molar ratio

Fig. 9. Conversions and H_2/CO for steam reforming. Experimental conditions: S/C = 0.88–1.77, T = 800–600°C, t_{red} = 4 h, WHSV = 328 m^3 hr^{-1} kg^{-1}.

$Mg_{0.4}Al_2O_{3.4}$ are unstable for TRM. Pure NiO, and 0.05 wt%Rh/$Mg_{1.1}Al_2O_{4.1}$ in combination with 5 wt%Ni/$Mg_{0.4}Al_2O_{3.4}$ showed a remarkable stability, however, NiO was only active for CH_4 combustion and not for SRM and DRM. According to them the main cause for deactivation was the formation of hot spot in the catalyst bed [38]. A high O/C results in high heat of reaction and thus leads to the formation of hot spots at the bed inlet. In the present study as we employed a differential reactor setup and limited the O/C to 0.2. It is to be noted that the molar ratio of N_2/O_2 used in this study is lower than that of air composition. In contrast, Luneau et al. replicated the inlet molar ratio of N_2/O_2 equivalent to air composition [38]. A similar work on TRM by Garcia-Vargas et al. showed a comparable X_{CO_2} = 33.7–63.5% [17] but a high X_{CO_2} = 87.82–90.20% is reported by Vital et al. for a feed composition of CH_4/CO_2 = 1.5, S/C = 0.3, and O/C = 0.1 [23]. Such high X_{CO_2} is mainly because of very low S/C = 0.3 employed, however, this results in a low H_2/CO = 1.33–1.43. Thus the quality of biogas has a profound impact on achievable X_{CO_2} and H_2/CO ratio in relation to the tunable oxidizer content. Though TRM resulted in an equilibrium CO_2 composition, the X_{CH_4} is still away from equilibrium. CH_4, despite being a limiting reactant with respect to overall oxidant concentrations (O_2 +H_2O+CO_2), the observed X_{CH_4} = 84.21–94.52% at 800°C is still below equilibrium conversion, which essentially means the residence time is not enough to achieve equilibrium conversion.

The effect of oxidizers content in different proportions shown in Fig. 11(a)-(c) can be summarized as follows.

- For any given S/C, an increase in O/C results in higher X_{CH_4}
  - This is an expected observation as an increase in oxidizer content will lead to higher X_{CH_4}. However, the mechanistic details of this behavior can be quite intriguing. Any carbon deposited may be gasified by oxygen, thus clearing the surface for further CH_4 adsorption and conversion. Another argument often discussed in the literature is that oxygen participates through indirect oxidation. This requires the complete combustion of CH_4 at the bed inlet to form CO_2 and H_2O followed by the reforming of the remaining CH_4 [71]. Since a differential reactor setup is used in the present study we can't adjudge the occurrence of this phenomenon.
- For any given O/C, an increase in S/C results in slightly higher X_{CH_4}
  - This is again an expected behavior as the increased partial pressure of steam results in higher X_{CH_4} as long as the WHSV is moderately low (high catalyst loading) to avoid deactivation.
- For any given S/C, an increase in O/C results in lower X_{CO_2}
  - The most likely reason for the decrease in X_{CO_2} is the oxidation of carbon or CO by oxygen, leading to the formation of CO_2. Any possibility of CO_2 formation from WGSR can be ignored in this case since the H_2/CO ratio decreases with an increase in O/C (Fig. 11

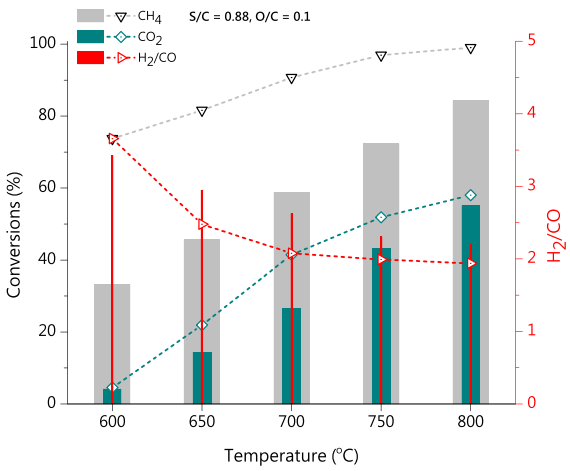

(a) T vs X_{CH_4}, X_{CO_2}, H_2/CO

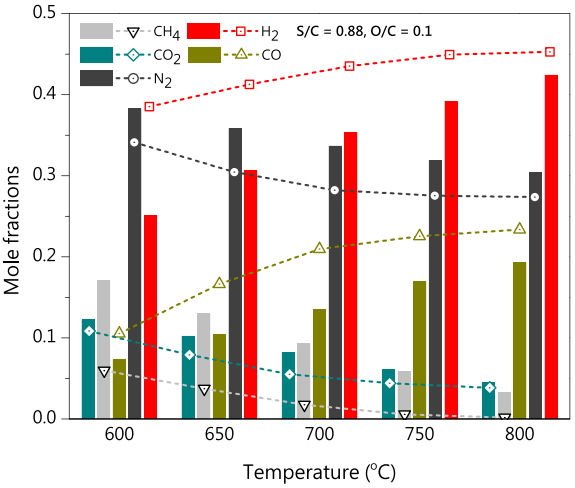

(b) T vs exit mole fractions

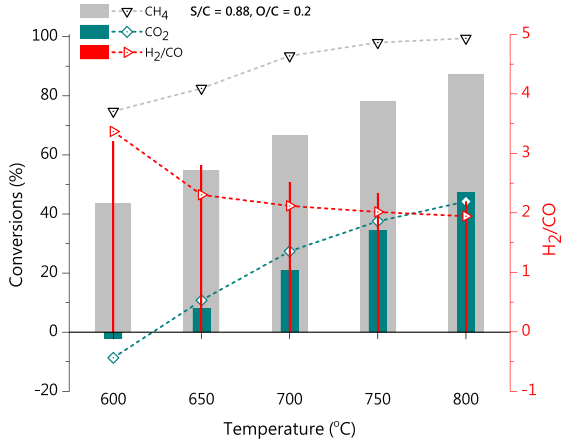

(c) T vs X_{CH_4}, X_{CO_2}, H_2/CO

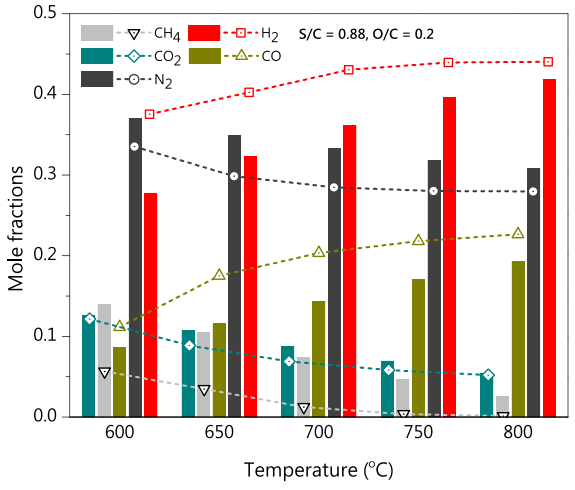

(d) T vs exit mole fractions

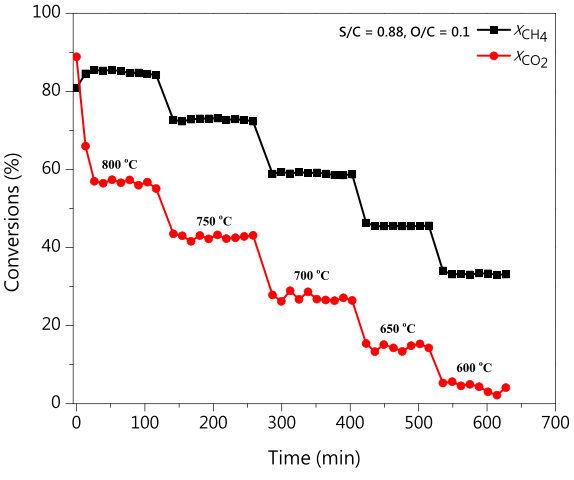

(e) Time vs X_{CH_4}, X_{CO_2}

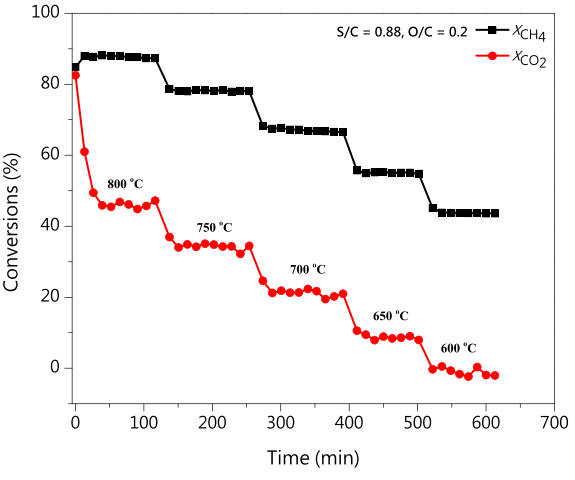

(f) Time vs X_{CH_4}, X_{CO_2}

Fig. 10. Conversions, exit mole fractions and H_2/CO for tri-reforming. Experimental conditions: $CH_4/CO_2 = 2$, S/C = 0.88, O/C = 0.1 & 0.2, T = 800–600°C, t_{red} = 4 h, WHSV = 336 $m^3\ hr^{-1}\ kg^{-1}$, (a)-(d) Comparison with equilibrium predictions (dashed lines with points represent equilibrium values).

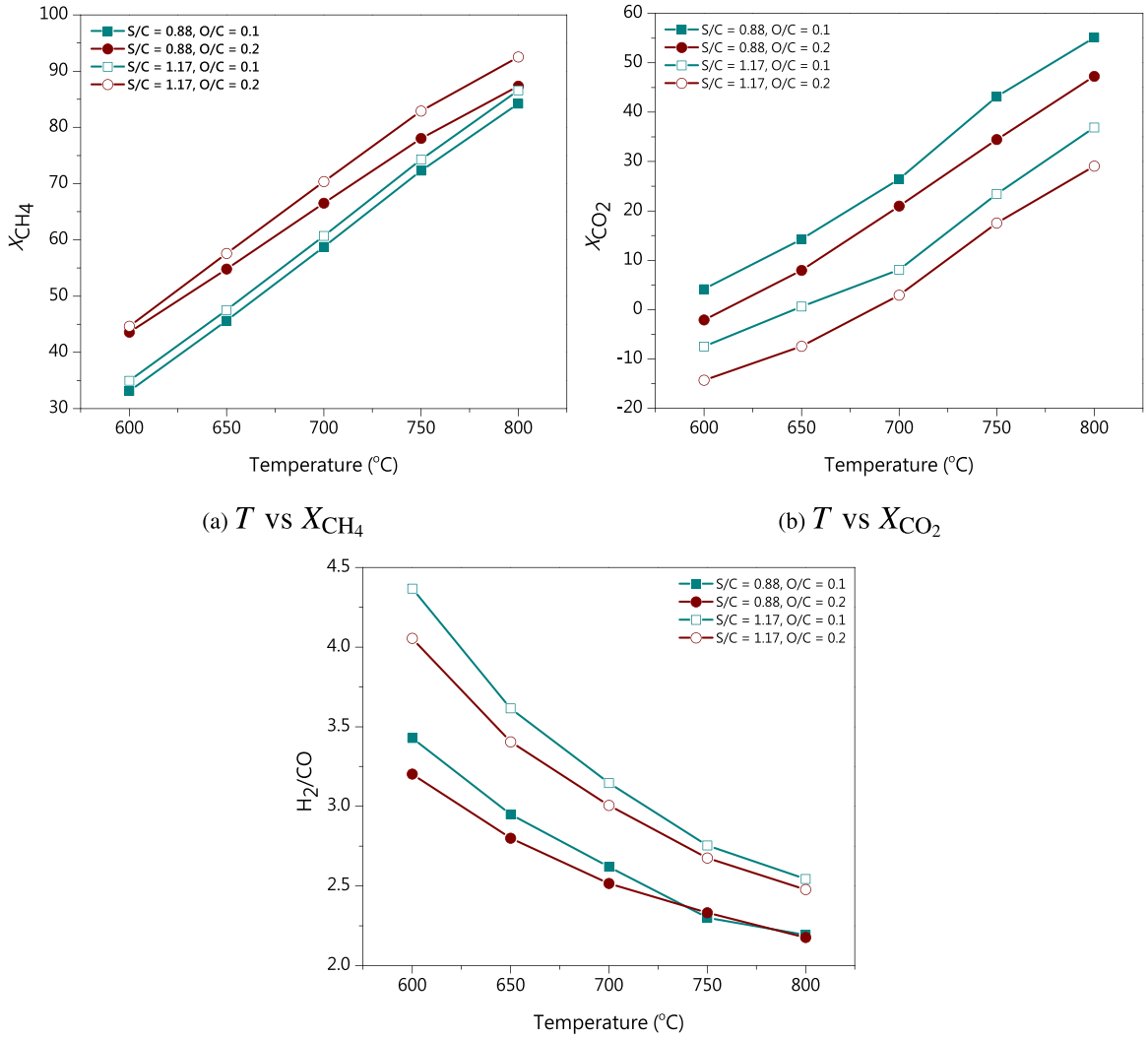

Fig. 11. Conversions and H_2/CO at different S/C and O/C for tri-reforming. Experimental conditions: $CH_4/CO_2 = 2$, S/C = 0.88 & 1.17, O/C = 0.1 & 0.2, T = 800–600°C, t_{red} = 4 h, WHSV = 336 $m^3\ hr^{-1}\ kg^{-1}$.

(c)). Had the source of CO_2 been WGSR, then the H_2/CO ratio must also increase with the increase in O/C, which is not the case here.

- For any given O/C, an increase in S/C results in lower X_{CO_2}
  - Analysis of Fig. 11(c) clearly shows that as the S/C ratio increases for a given O/C, the H_2/CO ratio increases, and the increase is significant at lower temperatures compared to higher temperatures. This is a clear indication of WGSR. Furthermore, X_{CO_2} is negative at lower temperatures. i.e., more CO_2 comes out of the reactor than what was initially present. Another reaction that can contribute to the formation of CO_2 is steam gasification of carbon. However, this reaction is favored at higher temperatures than at lower temperatures, and therefore, the lower X_{CO_2} observed is due to the production of CO_2 from WGSR.

The increased stability of the catalyst at temperature (800°C), when compared to CSDRM and SRM, may also be due to the oxidation-reduction redispersion phenomenon [32]. During the oxidation cycle, metal mobilization occurs due to the formation of metal oxide. Thereafter reduction in the H_2 environment results in catalytically active metal and this process can be termed as in situ oxidation and reduction process. The mobilization/redispersion is explained by the strain model as follows [34,72].

- Agglomerated large metal particles undergo oxidation resulting in oxymetal species on the surface of the particle.
- These complexes formed at the interface of metal-support induce strain in the metal which increases the free energy of the metal oxide surface layer compared to the unoxidized metal [34]. Consequently, these oxymetal species undergo progressive fragmentation from larger particles.
- Fragmented oxymetal undergoes redispersion through the interaction with the support structure.

The short-term deactivation of the catalyst observed in SRM and CSDRM can be addressed by the addition of small amounts of oxygen in the feed stream. The in situ oxidation and reduction cycles result in better catalyst stability as observed for all tested conditions. Accordingly, the process parameters of S/C = 0.88 and O/C = 0.1 resulted in a X_{CH_4} = 84.20% and X_{CH_4} = 55.13% at 800°C. While the corresponding H_2/CO = 2.19 is suitable for FT-Chemistry.

Finally, the significance of TRM over the other CH_4 reforming reactions is compared in Fig. 12. Adding steam and oxygen to the DRM increased X_{CH_4} from 28.41% to 84.20%, however, the X_{CO_2} dropped from 85.63% to 55.13%. The reasons for this drop are multifold, ranging from the occurrence of WGSR to carbon gasification. Comparison of X_{CO_2}

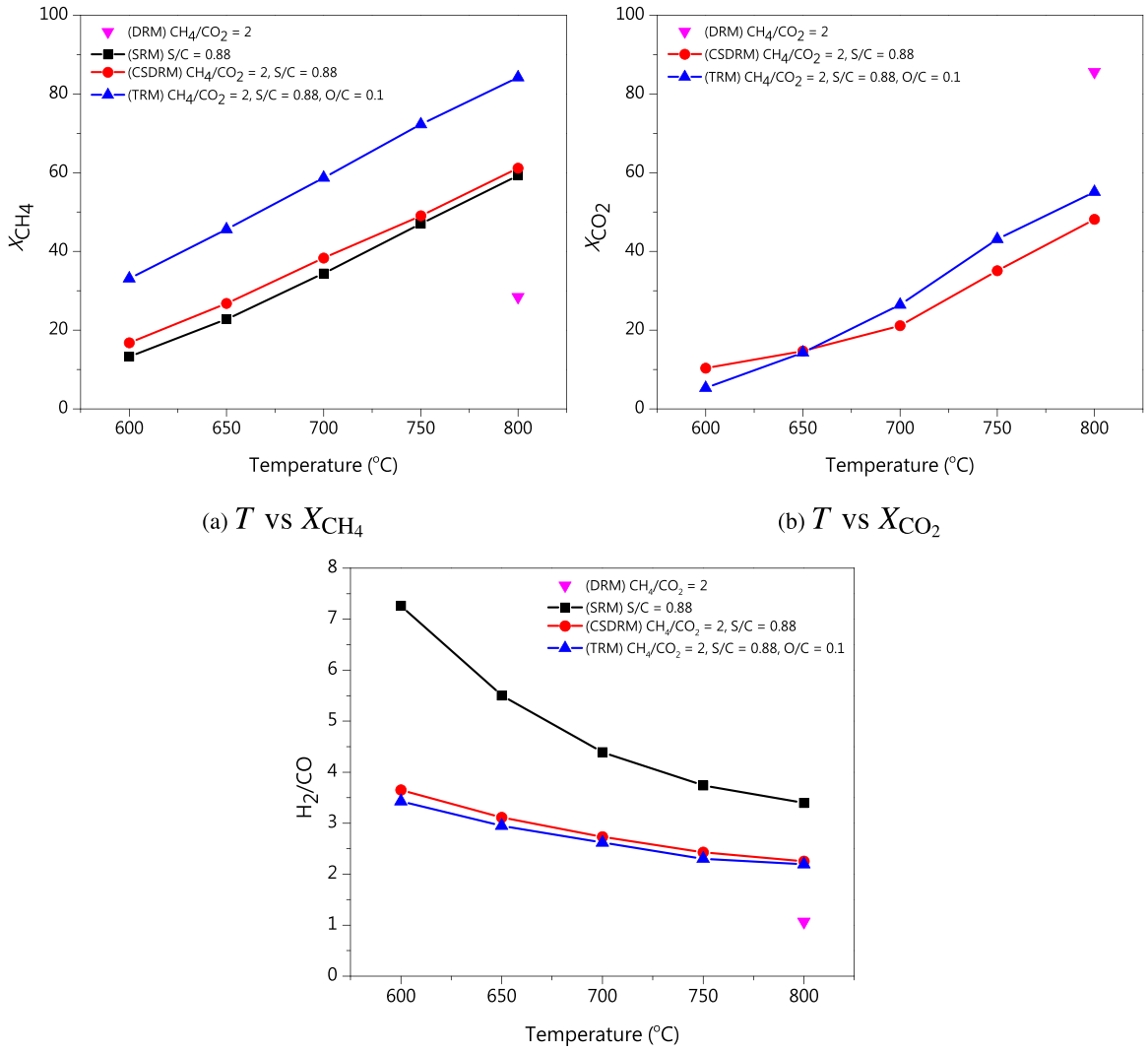

(a) T vs X_{CH_4}

(b) T vs X_{CO_2}

(c) T vs H_2/CO

Fig. 12. CH_4 reforming comparisons. Experimental conditions: T = 800–600°C, t_{red} = 4 h, WHSV = 336 $m^3\ hr^{-1}\ kg^{-1}$. For SRM reaction WHSV = 328 $m^3\ hr^{-1}\ kg^{-1}$.

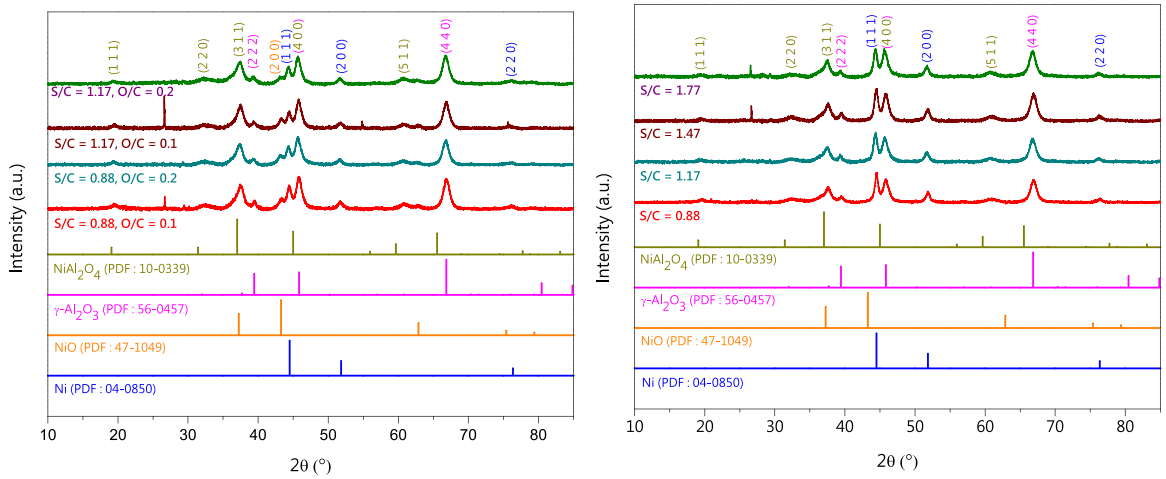

(a) XRD of TRM spent catalysts

(b) XRD of SRM spent catalysts

Fig. 13. XRD pattern of spent catalysts for TRM and SRM.

between CSDRM and TRM in Fig. 12(b) shows that addition of O_2 results in higher X_{CO_2} at higher temperatures. This could be due to the initial deactivation of the catalyst in the case of CSDRM as observed in Fig. 7 (e). From equilibrium calculations it can be seen that addition of O_2 decreases the X_{CO_2} (cf. Fig. S4) for TRM, and the same is observed in the case of experiments as well (Fig. 11). Analysis of H_2/CO ratios obtained from the CSDRM and TRM concludes that the addition of small amounts of O_2 does not alter the H_2/CO ratio at high temperatures but increases the X_{CH_4} from 61.17% to 84.20%, and improves the catalyst stability, which establishes TRM as better processing method over other CH_4 reforming methods.

3.3. Spent catalysts characterizations

Spent catalysts have been characterized for the structural and chemical changes induced as a result of reaction using XRD, XPS, TGA, and TEM. It has been established that operating under high S/C ratios, catalyst suffers deactivation resulting in an appreciable drop in X_{CH_4} on time on stream, especially at $T = 800$°C. Figure 13 represents the spent catalysts XRD for TRM and SRM, while Fig. S15 indicates the spectra of CSDRM.

XRD characterization of spent SRM samples has exhibited a noticeable increase in the intensity of characteristic $NiAl_2O_4$ reflection at $2\theta = 37°$. This observation is further correlated with the decrease in the ratio I_2 and a slight deviation in the experimentally observed lattice parameters. In particular, for the S/C = 1.17 and 1.77, I_2 decreases from 2.03 to 1.76 which indicates Ni dissolution into the γ-Al_2O_3 crystal lattice to form $NiAl_2O_4$, furthermore, the observed lattice parameters increased from 7.927 Å to 7.953 Å. Though this change is very small, it is to be noted that the lattice parameter of ≈ 7.95 is neither close to 7.911 Å (γ-Al_2O_3) nor 8.04 Å ($NiAl_2O_4$) which indicates spinel coexisting with alumina. From the surface chemical analysis of the same samples performed using XPS as shown in Fig. 14 it can be inferred that intensities of the Ni^{2+}_{Tetra} have increased, insinuating the formation of MSI through normal spinel. These observations from XRD and XPS fall in line with the steam-induced metal support interaction postulate of Sehested et al. in the formation of $NiAl_2O_4$ [29]. In the case of CSDRM, except for S/C = 0.88, the I_2 ratio decreased for S/C = 1.17–1.77 again in concurrence with increasing lattice parameters. For the particular case of S/C = 1.77, the observed lattice parameter is 7.97 Å. Correspondingly from the XPS analysis, the intensity of Ni^{2+}_{Tetra} as shown in Fig. 14 increased with an increase in S/C ratio, thus augmenting the postulate of increased MSI through the spinel formation rendering the Ni catalyst inactive.

In the case of TRM, the diffraction pattern showed a new reflection compared to SRM and CSDRM at $2\theta = 43.27$, which is the characteristic signature of the NiO(200) facet as shown in Fig. 13(a). Kim et al. [73] also observed the re-oxidation of metallic nickel, especially even at a very low O/C (≈ 0.1) ratio. To further confirm the formation of NiO, the spent catalyst of TRM reaction conducted at O/C = 0.1 and S/C = 1.17 is characterized by XPS analysis. Pure NiO exhibits a peak at 854.4 eV. As in the case of TRM, the XPS result shown in Fig. 14 exhibits a distinctive peak at 854.45 eV, a clear indication of NiO formation in line with the respective diffraction spectra. Furthermore, from the XPS analysis of the reaction samples of SRM and CSDRM, it can be inferred that the deactivation of the catalyst is not linked to the metallic nickel re-oxidation. Among all the tested reforming reactions, the TRM resulted in a very low ratio of I_2 (0.66–0.89) and a noticeable increase in lattice parameters ≈ 7.95–7.99 Å. Yet, the TRM exhibits a stable catalytic activity which can be explained by the in situ oxidation-reduction process happening in the O_2 +H_2 reaction environment. Coke removal by O_2 is another mechanism that improves the catalyst stability. Despite performing reactions at high oxidizing conditions, there is a clear deposition of carbon ($2\theta = 26.54$), as shown in Figs. 13, and S15.

To infer the effect of operating conditions on the carbon formation, thermogravimetric analysis of spent catalysts is performed in the O_2 atmosphere, and the results are shown in Fig. 15. The initial drop in weight till ≈ 300°C is associated with physical and structurally bound water. This is followed by a sharp weight gain in all catalysts, including the freshly reduced sample. The surface nickel oxidation phenomenon can be attributed to this observed weight gain in the range of 250–350°C. As with the case of DRM, SRM, and CSDRM, the TGA studies showed a plateau followed by weight loss starting from 450°C. The occurrence of such a weight loss observed till 650°C is mainly because of the oxidation of filamentous (C_α) and graphitic (C_β) carbon [74]. Among the conducted reactions, the weight loss due to carbon oxidation is highest for DRM, while the TRM with minimum oxygen content (O/C = 0.1) hindered the carbon deactivation of the catalyst. A comparison of CSDRM and TRM shows the positive effect of O_2 in reducing/mitigating carbon deposition. An interesting observation from the TGA studies is the weight gain noticed after 600°C even in the case of TRM and freshly reduced catalyst which is due to high temperature oxidation of Ni [75, 76]. High-temperature oxidation of metal requires the transportation of either O_2 or metal through the already formed oxide scale/layers. Mrowec et al. conducted nickel oxidation studies in the range of

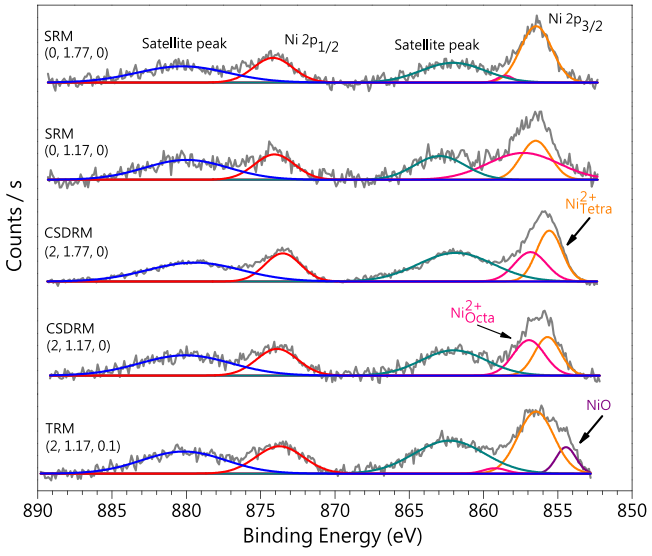

Fig. 14. XPS of post-reaction samples. Reaction conditions represented as (CH_4/CO_2, S/C, O/C).

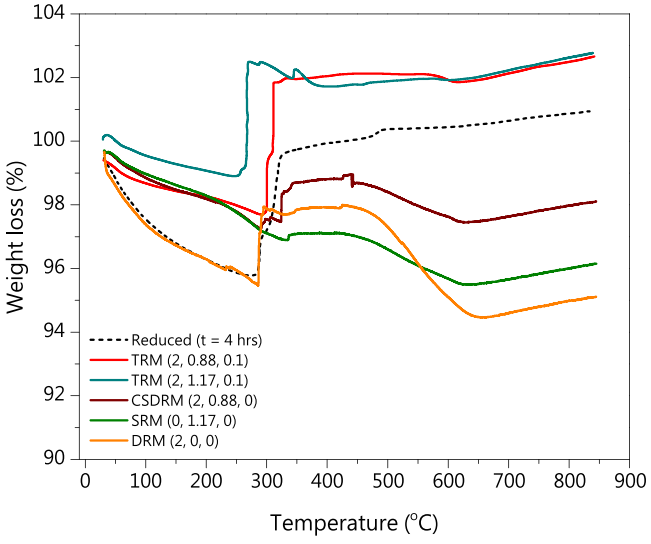

Fig. 15. Thermogravimetric analysis of reduced and spent samples. Reaction conditions represented as (CH_4/CO_2, S/C, O/C).

600–900°C and concluded that the weight gain below 800°C follows the parabolic law with the oxide scale growth, which is attributed to the outward diffusion of the nickel. In contrast, the diffusion of the O_2 dominates above 800°C [75].

From the post-catalytic XRD, XPS, and TGA characterizations of SRM, CSDRM, and TRM, it has been observed that nickel re-oxidation is not the reason for catalysts deactivation; instead, carbon deposition and formation of spinel structure are adjudged as the reasons. As pointed out by Ubaid et al., in nickel-deficient spinel structures, the deactivation of catalysts is due to the spinel formation without the detection of NiO [39]. Accordingly, in the present study of SRM and CSDRM, the absence of NiO is supported by the XRD and XPS analysis (cf. Figs. 13(b), S15, 14). While in the case of TRM, spent catalysts XRD and XPS characterizations clearly showed the formation of NiO (cf. Figs. 13(a), 14). In spite of the formation of NiO in TRM, the catalytic activity showed no transient behavior like in the case of SRM and CSDRM. This augments the positive effect of the addition of O_2 or the formation of NiO on the observed stable catalytic activity in TRM. Thus to understand the observed catalytic activity, the nature of active sites for CPoX, SRM, and DRM needs to be understood. Accordingly, the recent work of Luneau et al. on auto-thermal reforming of model-biogas reported that the NiO is active and stable for CH_4 combustion while inactive for SRM and DRM [38]. Apart from this, Rogers et al. studied the effect of the nature of active sites for SRM and DRM on Ni-deficient ($NiAl_4O_7$), stoichiometric ($NiAl_2O_4$), and excess-Ni ($Ni_2Al_2O_5$) spinels prepared using Pechini method [70]. Results on Ni-deficient spinel indicated that for DRM the reduced and unreduced $NiAl_4O_7$ is active while for SRM the reduced $NiAl_4O_7$ is active and the unreduced one is inactive. Since the prepared catalyst is Ni-deficient in the present study, we extend the results of Ubaid et al., Luneau et al., and Rogers et al. to explain the observed kinetics of our reaction systems.

Accordingly, we postulate that NiO formation is an active site for CH_4 combustion in TRM. In its reduced or unreduced form, the Ni-deficient spinel enhances the DRM, while the reduced Ni sites (cf. Fig. 13(a)) participate in the SRM. The presence of O_2 in the system will in turn oxidize the active Ni to NiO. Further, this NiO is reduced in situ because of the H_2 produced from reforming reactions. This leads to a dynamic equilibrium between the formation of active sites NiO and Ni in the case of TRM. Now if we consider the case of CSDRM, starting with a reduced catalyst both SRM and DRM are active. The presence of H_2O reintroduces the Ni into the spinel but this could be regenerated with H_2 produced from reforming reactions and the formed spinel is also active for DRM. Thus the same catalyst used for TRM should also be active for CSDRM. Instead, the catalyst's deactivation was observed in CSDRM, which could be due to the carbon deposition and/or nickel nano-particle sintering. Accordingly, the spent catalyst TGA characterization of CSDRM and SRM confirmed the carbon deposition (cf. Fig. 15). Thus the addition of O_2 in small quantities reduced/mitigated the carbon deposition (cf. Fig. 15) and possibly hindered the Ni sintering through in situ O_2/H_2 process as previously explained by the strain model in the TRM.

Further, to study the effect of nickel sintering in a high steam environment, standalone SRM experiments were conducted at S/C = 1.17, 1.77, 0.88 and T = 800°C. The obtained spent catalysts were subjected to TEM and XRD analysis, and the results are shown in Figs. 16 and 17. The experiments at S/C= 0.88 was done only for 3 h duration and therefore, the results of the spent catalyst characterizations for S/C= 0.88 are not shown in Figs. 16 and 17. Samples at S/C = 1.17 and S/C = 1.77, show identical XRD patterns confirming that the samples are multi-component systems composed of Ni (04–0850), $NiAl_2O4$ (10–0339), and γ-Al_2O_3 (56–0457). The only difference is a slight variation in the intensity ratio between Ni(111) and $NiAl_2O_4$(400) reflections. Compared to S/C = 1.17, S/C = 1.77 has a lower intensity for Ni(111). This implies lower pure Ni content in the latter, accounting for the lower catalytic activity in high S/C feed conditions. XRD pattern of the TRM (S/C = 0.88, O/C = 0.1) sample shows the presence of NiO in addition to Ni, $NiAl_2O_4$ and γ-Al_2O_3 which is due to the formation of NiO

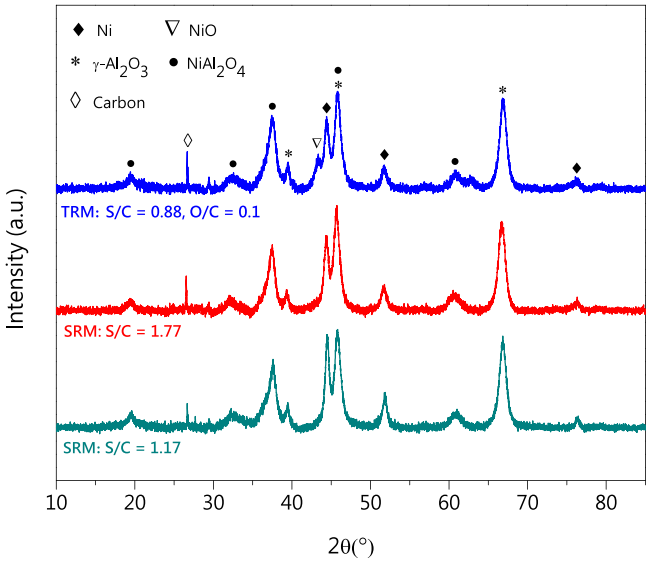

Fig. 16. XRD spectra of SRM and TRM spent catalysts at T = 800°C.

in the presence of O_2 in the feed. Though Ni in metallic form is present in all catalysts, from the ratio of peak intensities, it could be inferred that the available Ni active centers are more in the case of S/C = 1.17, which accounts for its superior activity over S/C = 1.77. In TRM (S/C = 0.88, O/C = 0.1), the better activity could also be attributed to the redispersion of surface Ni active centers aided by the formation of the NiO phase due to the presence of oxygen in the feed [77]. The average particle size of metallic Ni was calculated from XRD using the Scherrer equation from the Ni(111) peak of the samples and shown in Table 7.

Transmission electron microscopy (TEM) analysis of SRM and TRM samples is shown in Fig. 17. The average particle size calculated from the TEM images are also presented in Table 7. It is evident from TEM images that average particle size increases with an increase in S/C ratio from S/C = 1.17 (11.7 nm) to S/C = 1.77 (15.1 nm). This increase in the size of active catalytic nickel nanoparticles accounts for the lower catalytic activity in high steam feed conditions [78].

Though the average particle size distribution calculated from XRD analysis does not necessarily show a considerable change in the particle size between S/C = 1.17 to S/C = 1.77, analysis of multiple TEM images showed an appreciable variation.

A high-resolution transmission electron microscopy (HR-TEM) analysis was carried out to further understand the structure and particle size-driven catalytic activity. The HR-TEM image of the sample S/C= 1.17 at 800°C, is shown in Fig. 17(d). The sample indicates the presence of multiple crystalline phases. The dark high contrast region shows a lattice spacing of 0.173 nm corresponding to the (200) plane of Ni, and the **d** spacing value of 0.242 nm corresponds to the (311) lattice plane of the spinel structure, $NiAl_2O_4$. The presence of alumina is confirmed by the lattice spacing of 0.138 nm corresponding to the (440) crystal plane of γ-Al_2O_3 [79]. No **d** spacing value related to the NiO phase is observed in the HRTEM analysis of sample S/C = 1.17. Figure 17(e) represents the HR-TEM image of sample, S/C= 1.77. Interplanar distances of 0.173 nm, 0.242 nm, and 0.143 nm correspond to Ni(200), $NiAl_2O_4$(311), and NiO(220). Though the XRD pattern of S/C = 1.77 did not have peaks corresponding to NiO, the HR-TEM image accounts for the presence of an appreciable but quantitatively less NiO phase. For this deactivated catalyst, upon analyzing multiple images, the presence of graphitic carbon is also observed. The inset in Fig. 17(e) shows a lattice spacing of 0.317 nm corresponding to the (002) plane of graphitic carbon. The inset in Fig. 17(e) is the high-resolution image from the area highlighted in Fig. 17(b). The lattice spacing of 0.317 nm is for the fiber-like carbon growth. At the upper end of the graphitic carbon fiber **d** spacing of 0.173 nm was observed for a nanoparticle. This

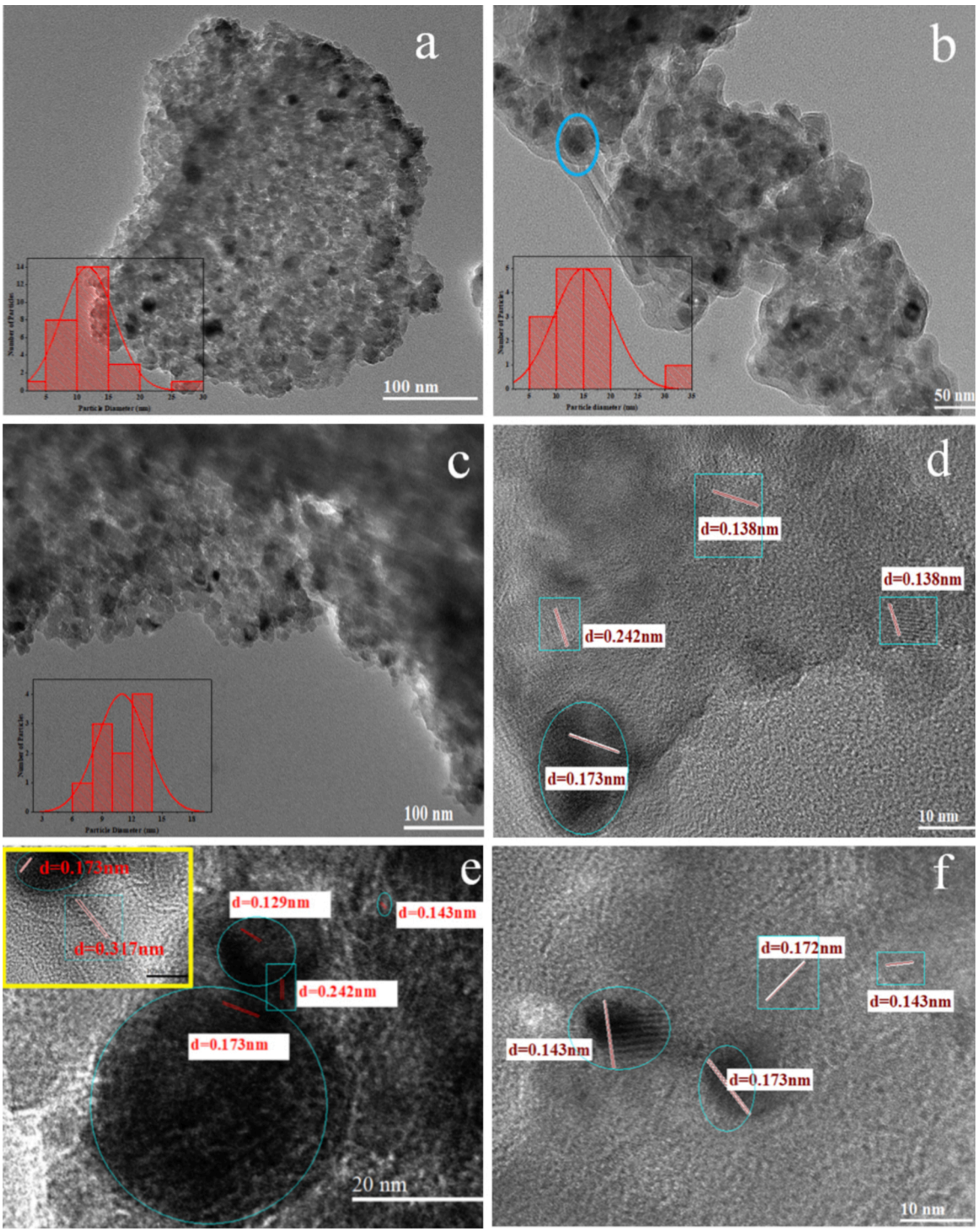

Fig. 17. TEM images of catalysts (a) SRM: S/C = 1.17, (b) SRM: S/C = 1.77 and (c) TRM: S/C = 0.88, O/C = 0.1. HR-TEM images of (d) SRM: S/C = 1.17, (e) SRM: S/C = 1.77 and (f) TRM: S/C = 0.88, O/C = 0.1. The inset in figure (e) is the HR-TEM image of the highlighted region in figure (b).

corresponds to the (200) plane of metallic nickel. On closer inspection of TEM images of S/C = 1.77, the sample is found to be covered by a layer of amorphous carbon, and it encapsulates the catalytic material. Loss of active nickel sites with amorphous carbon coupled with the presence of NiO phase leads to loss of activity in the catalyst S/C = 1.77. Fig. 17(f) represents the HR-TEM image of sample TRM (S/C = 0.88, O/C = 0.1). The lattice spacings 0.143 nm and 0.172 nm correspond to (220) of NiO and (200) of Ni. The HR-TEM images agree well with the XRD results. The activity or loss of activity of Ni@$NiAl_2O_4$ catalysts not only depends on coke formation but also on the distribution of catalytically active nickel sites on the support. Catalytic activity loss due to coke formation can be reversed by passing O_2. Analogously, the sintered catalyst regeneration could be achieved by repeated cycles of reaction with O_2 and H_2 as suggested by LaGrow et al [32]. This leads to the formation of catalytically less/non-active NiO phase (for SRM, DRM) but also aids in the dispersion of active nickel sites by reducing particle size as explained by the strain model or form the work of LaGrow et al [32,72]. In the present study, the loss of catalytic activity in CSDRM can be regenerated by adding O_2 which redisperses the sintered nickel with the aid of H_2 produced in TRM, and also the carbon deposition can be mitigated.

Table 7
Calculated particle size from XRD and TEM.

Catalyst	Avg particle size XRD (nm)	Avg particle size TEM (nm)
SRM (S/C = 1.17)	14.1	11.7
SRM (S/C = 1.77)	14.2	15.1
SRM (S/C = 0.88)	13.3	–
TRM (S/C = 0.88, O/C = 0.1)	11.1	10.9
Reduced catalyst (t_{red} = 4 h)	11.5	–

Accordingly, a stable catalytic activity was observed in the case of TRM.

4. Conclusions

Different reforming reactions (DRM, SRM, CSDRM, and TRM) were studied to investigate sustainable biogas utilization. Identification of optimal feed conditions (H_2O/CH_4 (S/C), O_2/CH_4 (O/C)) and reaction temperature (T) was achieved by performing chemical equilibrium analysis for a fixed synthetic biogas composition of 66.67% CH_4 and 33.33% CO_2. 10 wt% Ni/γ-Al_2O_3 is synthesized using the modified Pechini (sol-gel) method, and the optimal parameters necessary for the complete metal chelation were calculated using Visual MINTEQ speciation software.

The synthesized catalyst has shown a high degree of MSI due to the formation of nickel aluminate ($NiAl_2O_4$) when calcined at 800°C. From the effect of reduction time (t_{red}) studies, it was identified that for the nickel to exsolve from the $NiAl_2O_4$ high t_{red} and a reduction temperature of 800°C is required. Through residence time studies, it was observed that at high WHSV (336 $m^3\ hr^{-1}\ kg^{-1}$) (or low residence time) the effect of t_{red} was more pronounced as the kinetics of reactions were away from equilibrium, while low WHSV's (168, 84) (or high residence time) resulted in maximum allowable conversions (X_{CH_4}, X_{CO_2}) irrespective of t_{red} for CSDRM. Accordingly, a t_{red} = 4 h had a positive effect on the CSDRM when operated at S/C = 0.88, T = 800°C, and low residence time. The enhanced reaction kinetics was attributed to the increased surface nickel concentration mainly due to the contribution from tetrahedrally coordinated nickel (or normal spinel) due to the prolonged reduction in H_2 as confirmed by the XPS studies.

Reforming studies conducted in the presence of steam, particularly in the case of CSDRM and SRM with a WHSV = 336 $m^3\ hr^{-1}\ kg^{-1}$ showed catalyst deactivation on time-on-stream, particularly at high temperature. From the deactivation studies, it was distinguished that S/C had a direct correlation to the observed deactivation rates. An increase in the S/C ratio resulted in high X_{CH_4} and H_2/CO in SRM and CSDRM; however, X_{CO_2} decreased possibly due to the ready adsorption of H_2O over CO_2 onto the support and occurrence of WGSR. Spent catalyst characterizations revealed that the deactivation in the presence of high steam content is mainly due to the steam-induced metal support interaction resulting in an inactive spinel phase and not because of the metal re-oxidation as confirmed by the XRD and XPS. In the case of TRM reaction, the presence of O_2 even in a small quantity (O/C = 0.1) resulted in a stable catalytic activity at 800°C over the time on stream reported in this study despite the observed nickel re-oxidation through XRD and XPS characterizations. Thus confirming the importance of O_2 as an oxidizer in conducting the methane reforming reactions at high space velocities without losing the catalytic activity. The distinguishable stable TRM operation was mainly due to the in situ metal redispersion phenomenon enhanced mainly due to the oxidation-reduction cycles and coke removal by O_2. Consequently, from the TEM analysis of SRM and TRM spent catalysts, the particle size increase was observed for the SRM (≈ 15.1 nm) compared to the TRM (≈ 10.9 nm), which augments the conclusion of metal sintering, thus deactivating the catalyst. So, the observed catalyst deactivation is due to carbon deposition and nickel sintering in steam environment [77]. As with the case of S/C, increasing the O/C ratio also resulted in a high X_{CH_4} while X_{CO_2} decreased. Finally, both CSDRM and TRM resulted in a syngas composition (H_2/CO = 2.19) that is suitable for Fisher-Tropsch chemistry.

CRediT authorship contribution statement

Prakash V. Ponugoti: Methodology, Investigation, Data curation, Validation, Writing - original draft, Visualization. **Priya Pathmanathan**: Resources, Visualization. **Jyotsna Rapolu**: Resources. **A. Gomathi**: Resources, Data curation, Visualization, Writing - review & editing, Supervision. **Vinod M. Janardhanan**: Conceptualization, Writing - review & editing, Supervision, Project administration, Funding acquisition.

Declaration of Competing Interest

The authors declare that they have no known competing financial interests or personal relationships that could have appeared to influence the work reported in this paper.

Data availability

Data will be made available on request.

Appendix A. Supporting information

Supplementary data associated with this article can be found in the online version at doi:10.1016/j.apcata.2023.119033.

References

[1] B. Tjaden, M. Gandiglio, A. Lanzini, M. Santarelli, M. Järvinen, Small-scale biogas-SOFC plant: technical analysis and assessment of different fuel reforming options, Energy Fuels 28 (2014) 4216–4232, https://doi.org/10.1021/ef500212j.
[2] X.H. Pham, U.P. Ashik, J.I. Hayashi, A. PérezAlonso, D. Pla, M. Gómez, D. PhamMinh, Review on the catalytic tri-reforming of methane - Part II: catalyst development, Appl. Catal., A 623 (2021), https://doi.org/10.1016/j.apcata.2021.118286.
[3] V.L. Dagle, C. Smith, M. Flake, K.O. Albrecht, M.J. Gray, K.K. Ramasamy, R. A. Dagle, Integrated process for the catalytic conversion of biomass-derived syngas into transportation fuels, Green. Chem. 18 (2016) 1880–1891, https://doi.org/10.1039/c5gc02298c.
[4] M. Gupta, M.L. Smith, J.J. Spivey, Heterogeneous catalytic conversion of dry syngas to ethanol and higher alcohols on Cu-based catalysts, ACS Catal. 1 (2011) 641–656, https://doi.org/10.1021/cs2001048.
[5] A. Molino, V. Larocca, S. Chianese, D. Musmarra, Biofuels production by biomass gasification: a review, Energies 11 (2018) 1–31, https://doi.org/10.3390/en11040811.
[6] K. Aasberg-Petersen, J.H. BakHansen, T.S. Christensen, I. Dybkjaer, P. S. Christensen, C. StubNielsen, S.E. WinterMadsen, J.R. Rostrup-Nielsen, Technologies for large-scale gas conversion, Appl. Catal., A 221 (2001) 379–387, https://doi.org/10.1016/S0926-860X(01)00811-0.
[7] X. Song, Z. Guo, Technologies for direct production of flexible H_2/CO synthesis gas, Energy Convers Manage 47 (2006) 560–569, https://doi.org/10.1016/j.enconman.2005.05.012.
[8] U.S. Mohanty, M. Ali, M.R. Azhar, A. Al-Yaseri, A. Keshavarz, S. Iglauer, Current advances in syngas (CO + H_2) production through bi-reforming of methane using various catalysts: a review, Int. J. Hydrog. Energy 46 (2021) 32809–32845, https://doi.org/10.1016/j.ijhydene.2021.07.097.
[9] R.D. Alli, P.A. de Souza, M. Mohamedali, L.D. Virla, N. Mahinpey, Tri-reforming of methane for syngas production using Ni catalysts: current status and future outlook, Catal. Today 407 (2023) 107–124, https://doi.org/10.1016/j.cattod.2022.02.006.
[10] D. PhamMinh, X.H. Pham, T.J. Siang, D.V.N. Vo, Review on the catalytic tri-reforming of methane - Part I: Impact of operating conditions, catalyst deactivation and regeneration, Appl. Catal., A 621 (2021), 118202, https://doi.org/10.1016/j.apcata.2021.118202.
[11] J. Jeon, S. Nam, C.H. Ko, Rapid evaluation of coke resistance in catalysts for methane reforming using low steam-to-carbon ratio, Catal. Today 309 (2018) 140–146, https://doi.org/10.1016/j.cattod.2017.08.051.
[12] X. Guo, Y. Sun, Y. Yu, X. Zhu, C.J. Liu, Carbon formation and steam reforming of methane on silica supported nickel catalysts, Catal. Commun. 19 (2012) 61–65, https://doi.org/10.1016/j.catcom.2011.12.031.
[13] F. Meshkani, M. Rezaei, M. Andache, Investigation of the catalytic performance of Ni/MgO catalysts in partial oxidation, dry reforming and combined reforming of methane, J. Ind. Eng. Chem. 20 (2014) 1251–1260, https://doi.org/10.1016/j.jiec.2013.06.052.

[14] Y.A. Zhu, D. Chen, X.G. Zhou, W.K. Yuan, DFT studies of dry reforming of methane on Ni catalyst, Catal. Today 148 (2009) 260–267, https://doi.org/10.1016/j.cattod.2009.08.022.

[15] W. An, X.C. Zeng, C.H. Turner, First-principles study of methane dehydrogenation on a bimetallic Cu/Ni(111) surface, J. Chem. Phys. 131 (2009), https://doi.org/10.1063/1.3254383.

[16] J. Yoo, Y. Bang, S.J. Han, S. Park, J.H. Song, I.K. Song, Hydrogen production by tri-reforming of methane over nickel-alumina aerogel catalyst, J. Mol. Catal. A: Chem. 410 (2015) 74–80, https://doi.org/10.1016/j.molcata.2015.09.008.

[17] J.M. García-Vargas, J.L. Valverde, F. Dorado, P. Sánchez, Influence of the support on the catalytic behaviour of Ni catalysts for the dry reforming reaction and the tri-reforming process, J. Mol. Catal. A: Chem. 395 (2014) 108–116, https://doi.org/10.1016/j.molcata.2014.08.019.

[18] R. Kumar, K. Kumar, N.V. Choudary, K.K. Pant, Effect of support materials on the performance of Ni-based catalysts in tri-reforming of methane, Fuel Process. Technol. 186 (2019) 40–52, https://doi.org/10.1016/j.fuproc.2018.12.018.

[19] R. Kumar, K. Kumar, K.K. Pant, N.V. Choudary, Tuning the metal-support interaction of methane tri-reforming catalysts for industrial flue gas utilization, Int. J. Hydrog. Energy 45 (2020) 1911–1929, https://doi.org/10.1016/j.ijhydene.2019.11.111.

[20] K. Świrk, J. Grams, M. Motak, P. Da Costa, T. Grzybek, Understanding of tri-reforming of methane over Ni/Mg/Al hydrotalcite-derived catalyst for CO_2 utilization from flue gases from natural gas-fired power plants, J. CO_2 Util. 42 (2020) 1–7, https://doi.org/10.1016/j.jcou.2020.101317.

[21] C.G. Anchieta, E.M. Assaf, J.M. Assaf, Syngas production by methane tri-reforming: Effect of Ni/CeO_2 synthesis method on oxygen vacancies and coke formation, J. CO_2 Util. 56 (2022), https://doi.org/10.1016/j.jcou.2021.101853.

[22] C.G. Anchieta, E.M. Assaf, J.M. Assaf, Effect of ionic liquid in Ni/ZrO_2 catalysts applied to syngas production by methane tri-reforming, Int. J. Hydrog. Energy 44 (2019) 9316–9327, https://doi.org/10.1016/j.ijhydene.2019.02.122.

[23] A. Vita, L. Pino, F. Cipitì, M. Laganà, V. Recupero, Biogas as renewable raw material for syngas production by tri-reforming process over $NiCeO_2$ catalysts: optimal operative condition and effect of nickel content, Fuel Process. Technol. 127 (2014) 47–58, https://doi.org/10.1016/j.fuproc.2014.06.014.

[24] A.V. PaladinoLino, E.M. Assaf, J.M. Assaf, Adjusting process variables in methane tri-reforming to achieve suitable syngas quality and low coke deposition, Energy Fuels 34 (2020) 16522–16531, https://doi.org/10.1021/acs.energyfuels.0c02895.

[25] X. Zhai, S. Ding, Z. Liu, Y. Jin, Y. Cheng, Catalytic performance of Ni catalysts for steam reforming of methane at high space velocity, Int. J. Hydrog. Energy 36 (2011) 482–489, https://doi.org/10.1016/j.ijhydene.2010.10.053.

[26] D.H. Prasad, H.I. Ji, H.R. Kim, J.W. Son, B.K. Kim, H.W. Lee, J.H. Lee, Effect of nickel nano-particle sintering on methane reforming activity of Ni-CGO cermet anodes for internal steam reforming SOFCs, Appl. Catal., B 101 (2011) 531–539, https://doi.org/10.1016/j.apcatb.2010.10.026.

[27] D.H. Prasad, S.Y. Park, H. Ji, H.R. Kim, J.W. Son, B.K. Kim, H.W. Lee, J.H. Lee, Effect of steam content on nickel nano-particle sintering and methane reforming activity of Ni-CZO anode cermets for internal reforming SOFCs, Appl. Catal., A 411–412 (2012) 160–169, https://doi.org/10.1016/j.apcata.2011.10.035.

[28] J. Sehested, J.A. Gelten, I.N. Remediakis, H. Bengaard, J.K. Nørskov, Sintering of nickel steam-reforming catalysts: Effects of temperature and steam and hydrogen pressures, J. Catal. 223 (2004) 432–443, https://doi.org/10.1016/j.jcat.2004.01.026.

[29] J. Sehested, J.A. Gelten, S. Helveg, Sintering of nickel catalysts: effects of time, atmosphere, temperature, nickel-carrier interactions, and dopants, Appl. Catal., A 309 (2006) 237–246, https://doi.org/10.1016/j.apcata.2006.05.017.

[30] J. Sehested, Four challenges for nickel steam-reforming catalysts, Catal. Today 111 (2006) 103–110, https://doi.org/10.1016/j.cattod.2005.10.002.

[31] M. Wolf, Thermodynamic assessment of the stability of bulk and nanoparticulate cobalt and nickel during dry and steam reforming of methane, RSC Adv. 11 (2021) 18187–18197, https://doi.org/10.1039/d1ra01856f.

[32] A.P. LaGrow, D.C. Lloyd, P.L. Gai, E.D. Boyes, In situ scanning transmission electron microscopy of Ni nanoparticle redispersion via the reduction of hollow NiO, Chem. Mater. 30 (2018) 197–203, https://doi.org/10.1021/acs.chemmater.7b04184.

[33] H. Xie, M. Hong, E.M. Hitz, X. Wang, M. Cui, D.J. Kline, M.R. Zachariah, L. Hu, High-temperature pulse method for nanoparticle redispersion, J. Am. Chem. Soc. 142 (2020) 17364–17371, https://doi.org/10.1021/jacs.0c04887.

[34] K. Morgan, A. Goguet, C. Hardacre, Metal redispersion strategies for recycling of supported metal catalysts: a perspective, ACS Catal. 5 (2015) 3430–3445, https://doi.org/10.1021/acscatal.5b00535.

[35] F. Behafarid, S. Pandey, R.E. Diaz, E.A. Stach, B.R. Cuenya, An in situ transmission electron microscopy study of sintering and redispersion phenomena over size-selected metal nanoparticles: environmental effects, Phys. Chem. Chem. Phys. 16 (2014) 18176–18184, https://doi.org/10.1039/c4cp02574a.

[36] A.J. Majewski, J. Wood, Tri-reforming of methane over Ni@SiO_2 catalyst, Int. J. Hydrog. Energy 39 (2014) 12578–12585, https://doi.org/10.1016/j.ijhydene.2014.06.071.

[37] M. Luneau, Y. Schuurman, F.C. Meunier, C. Mirodatos, N. Guilhaume, High-throughput assessment of catalyst stability during autothermal reforming of model biogas, Catal. Sci. Technol. 5 (2015) 4390–4397, https://doi.org/10.1039/c5cy00702j.

[38] M. Luneau, E. Gianotti, F.C. Meunier, C. Mirodatos, E. Puzenat, Y. Schuurman, N. Guilhaume, Deactivation mechanism of Ni supported on Mg-Al spinel during autothermal reforming of model biogas, Appl. Catal., B 203 (2017) 289–299, https://doi.org/10.1016/j.apcatb.2016.10.023.

[39] A. Al-Ubaid, E.E. Wolf, Steam reforming of methane on reduced non-stoichiometric nickel aluminate catalysts, Appl. Catal. 40 (1988) 73–85, https://doi.org/10.1016/S0166-9834(00)80427-3.

[40] A. Heller, A. Barkleit, H. Foerstendorf, S. Tsushima, K. Heim, G. Bernhard, Curium (III) citrate speciation in biological systems: A europium(III) assisted spectroscopic and quantum chemical study, Dalton Trans. 41 (2012) 13969–13983, https://doi.org/10.1039/c2dt31480k.

[41] S.A. SeyyedEbrahimi, S.M. Masoudpanah, Effects of pH and citric acid content on the structure and magnetic properties of MnZn ferrite nanoparticles synthesized by a sol-gel autocombustion method, J. Magn. Magn. Mater. 357 (2014) 77–81, https://doi.org/10.1016/j.jmmm.2014.01.017.

[42] J.H. Choy, Y.S. Han, Citrate route to the piezoelectric Pb(Zr,Ti)O_3 oxide, J. Mater. Chem. 7 (1997) 1815–1820, https://doi.org/10.1039/a700687j.

[43] P. Kim, Y. Kim, H. Kim, I.K. Song, J. Yi, Synthesis and characterization of mesoporous alumina with nickel incorporated for use in the partial oxidation of methane into synthesis gas, Appl. Catal., A 272 (2004) 157–166, https://doi.org/10.1016/j.apcata.2004.05.055.

[44] L. Smoláková, M. Kout, E. Koudelková, L. Čapek, Effect of calcination temperature on the structure and catalytic performance of the Ni/Al_2 O_3 and Ni-Ce/Al_2 O_3 catalysts in oxidative dehydrogenation of ethane, Ind. Eng. Chem. Res. 54 (2015) 12730–12740, https://doi.org/10.1021/acs.iecr.5b03425.

[45] Z. Bian, W. Zhong, Y. Yu, Z. Wang, B. Jiang, S. Kawi, Dry reforming of methane on Ni/mesoporous-Al_2O_3 catalysts: effect of calcination temperature, Int. J. Hydrog. Energy 46 (2021) 31041–31053, https://doi.org/10.1016/j.ijhydene.2020.12.064.

[46] A.A. Gonçalves, M.J. Costa, L. Zhang, F. Ciesielczyk, M. Jaroniec, One-pot synthesis of $MeAl_2O_4$ (Me = Ni, Co, or Cu) supported on γ-Al_2O_3 with ultralarge mesopores: enhancing interfacial defects in γ-Al_2O_3 to facilitate the formation of spinel structures at lower temperatures, Chem. Mater. 30 (2018) 436–446, https://doi.org/10.1021/acs.chemmater.7b04353.

[47] Z. Alipour, M. Rezaei, F. Meshkani, Effect of Ni loadings on the activity and coke formation of MgO-modified Ni/Al_2O_3 nanocatalyst in dry reforming of methane, J. Energy Chem. 23 (2014) 633–638, https://doi.org/10.1016/S2095-4956(14)60194-7.

[48] P. Kumar, S.K. Maity, D. Shee, Hydrodeoxygenation of stearic acid using Mo modified Ni and Co/alumina catalysts: Effect of calcination temperature, Chem. Eng. Commun. 207 (2020) 904–919, https://doi.org/10.1080/00986445.2019.1630396.

[49] J.F. Hochepied, P. Nortier, Influence of precipitation conditions (pH and temperature) on the morphology and porosity of boehmite particles, Powder Technol. 128 (2002) 268–275, https://doi.org/10.1016/S0032-5910(02)00178-X.

[50] G. Zu, J. Shen, X. Wei, X. Ni, Z. Zhang, J. Wang, G. Liu, Preparation and characterization of monolithic alumina aerogels, J. Non-Cryst. Solids 357 (2011) 2903–2906, https://doi.org/10.1016/j.jnoncrysol.2011.03.031.

[51] Z. Zhong, Y. Mastai, Y. Koltypin, Y. Zhao, A. Gedanken, Sonochemical coating of nanosized nickel on alumina submicrospheres and the interaction between the nickel and nickel oxide with the substrate, Chem. Mater. 11 (1999) 2350–2359, https://doi.org/10.1021/cm981005m.

[52] C. Ragupathi, J.J. Vijaya, P. Surendhar, L.J. Kennedy, Comparative investigation of nickel aluminate ($NiAl_2O_4$) nano and microstructures for the structural, optical and catalytic properties, Polyhedron 72 (2014) 1–7, https://doi.org/10.1016/j.poly.2014.01.013.

[53] A. Irshad, M.F. Warsi, P.O. Agboola, G. Dastgeer, M. Shahid, Sol-gel assisted Ag doped $NiAl_2O_4$ nanomaterials and their nanocomposites with g-C_3N_4 nanosheets for the removal of organic effluents, J. Alloy. Compd. 902 (2022), https://doi.org/10.1016/j.jallcom.2022.163805.

[54] A.A. Gonçalves, M.J. Costa, L. Zhang, F. Ciesielczyk, M. Jaroniec, One-pot synthesis of $MeAl_2O_4$ (Me = Ni, Co, or Cu) supported on γ-Al_2O_3 with ultralarge mesopores: enhancing interfacial defects in γ-Al_2O_3 to facilitate the formation of spinel structures at lower temperatures, Chem. Mater. 30 (2018) 436–446, https://doi.org/10.1021/acs.chemmater.7b04353.

[55] N. Bayal, P. Jeevanandam, Synthesis of metal aluminate nanoparticles by sol-gel method and studies on their reactivity, J. Alloy. Compd. 516 (2012) 27–32, https://doi.org/10.1016/j.jallcom.2011.11.080.

[56] Y. Kathiraser, W. Thitsartarn, K. Sutthiumporn, S. Kawi, Inverse $NiAl_2O_4$ on $LaAlO_3$-Al_2O_3: unique catalytic structure for stable CO_2 reforming of methane, J. Phys. Chem. C. 117 (2013) 8120–8130, https://doi.org/10.1021/jp401855x.

[57] M. Wu, D.M. Hercules, Studies of supported nickel catalysts by X-ray photoelectron and ion scattering spectroscopies, J. Phys. Chem. 83 (1979) 2003–2008, https://doi.org/10.1021/j100478a015.

[58] D. Beierlein, D. Häussermann, M. Pfeifer, T. Schwarz, K. Stöwe, Y. Traa, E. Klemm, Is the CO_2 methanation on highly loaded Ni-Al_2O_3 catalysts really structure-sensitive? Appl. Catal., B 247 (2019) 200–219, https://doi.org/10.1016/j.apcatb.2018.12.064.

[59] V. Pawar, S. Appari, D.S. Monder, V.M. Janardhanan, Study of the combined deactivation due to sulfur poisoning and carbon deposition during biogas dry reforming on supported Ni catalyst, Ind. Eng. Chem. Res. 56 (2017) 8448–8455, https://doi.org/10.1021/acs.iecr.7b01662.

[60] S. Appari, V.M. Janardhanan, R. Bauri, S. Jayanti, Deactivation and regeneration of Ni catalyst during steam reforming of model biogas: An experimental investigation, Int. J. Hydrog. Energy 39 (2014) 297–304, https://doi.org/10.1016/j.ijhydene.2013.10.056.

[61] Jae Chul Ro, J.C. In, Structures and properties of silica gels prepared by the sol-gel method, J. Non-Cryst. Solids 130 (1991) 8–17, https://doi.org/10.1016/0022-3093(91)90151-U.

[62] A.P. Grosvenor, M.C. Biesinger, R.S.C. Smart, N.S. McIntyre, New interpretations of XPS spectra of nickel metal and oxides, Surf. Sci. 600 (2006) 1771–1779, https://doi.org/10.1016/j.susc.2006.01.041.
[63] A.A. Lemonidou, M.A. Goula, I.A. Vasalos, Carbon dioxide reforming of methane over 5 wt% nickel calcium aluminate catalysts - Effect of preparation method, Catal. Today 46 (1998) 175–183, https://doi.org/10.1016/S0920-5861(98)00339-3.
[64] D.M. Walker, S.L. Pettit, J.T. Wolan, J.N. Kuhn, Synthesis gas production to desired hydrogen to carbon monoxide ratios by tri-reforming of methane using Ni-MgO-(Ce,Zr)O_2 catalysts, Appl. Catal., A 445–446 (2012) 61–68, https://doi.org/10.1016/j.apcata.2012.08.015.
[65] N. Guilhaume, D. Bianchi, R.A. Wandawa, W. Yin, Y. Schuurman, Study of CO_2 and H_2O adsorption competition in the combined dry/steam reforming of biogas, Catal. Today 375 (2021) 282–289, https://doi.org/10.1016/j.cattod.2020.04.058.
[66] S. Singh, M.B. Bahari, B. Abdullah, P.T. Phuong, Q.D. Truong, D.V.N. Vo, A. A. Adesina, Bi-reforming of methane on Ni/SBA-15 catalyst for syngas production: Influence of feed composition, Int. J. Hydrog. Energy 43 (2018) 17230–17243, https://doi.org/10.1016/j.ijhydene.2018.07.136.
[67] A.L. Karemore, P.D. Vaidya, R. Sinha, P. Chugh, On the dry and mixed reforming of methane over Ni/Al_2O_3 - Influence of reaction variables on syngas production, Int. J. Hydrog. Energy 41 (2016) 22963–22975, https://doi.org/10.1016/j.ijhydene.2016.09.038.
[68] V. Pawar, D. Ray, C. Subrahmanyam, V.M. Janardhanan, Study of short-term catalyst deactivation due to carbon deposition during biogas dry reforming on supported Ni catalyst, Energy Fuels 29 (2015) 8047–8052, https://doi.org/10.1021/acs.energyfuels.5b01862.
[69] Z. Hou, J. Gao, J. Guo, D. Liang, H. Lou, X. Zheng, Deactivation of Ni catalysts during methane autothermal reforming with CO_2 and O_2 in a fluidized-bed reactor, J. Catal. 250 (2007) 331–341, https://doi.org/10.1016/j.jcat.2007.06.023.
[70] J.L. Rogers, M.C. Mangarella, A.D. D'Amico, J.R. Gallagher, M.R. Dutzer, E. Stavitski, J.T. Miller, C. Sievers, Differences in the nature of active sites for methane dry reforming and methane steam reforming over nickel aluminate catalysts, ACS Catal. 6 (2016) 5873–5886, https://doi.org/10.1021/acscatal.6b01133.
[71] K. HerreraDelgado, L. Maier, S. Tischer, A. Zellner, H. Stotz, O. Deutschmann, Surface reaction kinetics of steam- and CO_2 -reforming as well as oxidation of methane over nickel-based catalysts, Catalysts 5 (2015) 871–904, https://doi.org/10.3390/catal5020871.
[72] E. Ruckenstein, M.L. Malhotra, Splitting of platinum crystallites supported on thin, nonporous alumina films, J. Catal. 41 (1976) 303–311, https://doi.org/10.1016/0021-9517(76)90345-6.
[73] S. Kim, B.S. Crandall, M.J. Lance, N. Cordonnier, J. Lauterbach, E. Sasmaz, Activity and stability of NiCe@SiO_2 multi-yolk-shell nanotube catalyst for tri-reforming of methane, Appl. Catal., B 259 (2019), 118037, https://doi.org/10.1016/j.apcatb.2019.118037.
[74] I. Luisetto, S. Tuti, C. Battocchio, S. LoMastro, A. Sodo, Ni/CeO_2-Al_2O_3 catalysts for the dry reforming of methane: The effect of $CeAlO_3$ content and nickel crystallite size on catalytic activity and coke resistance, Appl. Catal., A 500 (2015) 12–22, https://doi.org/10.1016/j.apcata.2015.05.004.
[75] S. Mrowec, Z. Grzesik, Oxidation of nickel and transport properties of nickel oxide, J. Phys. Chem. Solids 65 (2004) 1651–1657, https://doi.org/10.1016/j.jpcs.2004.03.011.
[76] S. Chevalier, F. Desserrey, J.P. Larpin, Oxygen transport during the high temperature oxidation of pure nickel, Oxid. Met. 64 (2005) 219–234, https://doi.org/10.1007/s11085-005-6560-x.
[77] A. Remiro, A. Arandia, L. Oar-Arteta, J. Bilbao, A.G. Gayubo, Regeneration of $NiAl_2O_4$ spinel type catalysts used in the reforming of raw bio-oil, Appl. Catal., B 237 (2018) 353–365, https://doi.org/10.1016/j.apcatb.2018.06.005.
[78] Z.Y. Lim, C. Wu, W.G. Wang, K.L. Choy, H. Yin, A novel and anti-agglomerating Ni@yolk-ZrO_2 structure with sub-10 nm Ni core for high performance steam reforming of methane, RSC Adv. 5 (2015) 61925–61932, https://doi.org/10.1039/c5ra10493a.
[79] J.R. Ross, M.C. Steel, A. Zeini-Isfahani, Evidence for the participation of surface nickel aluminate sites in the steam reforming of methane over nickel/alumina catalysts, J. Catal. 52 (1978) 280–290, https://doi.org/10.1016/0021-9517(78)90142-2.